












# Live imaging of neolymphangiogenesis identifies acute antimetastatic roles of dsRNA mimics

David Olmeda<sup>1,\*</sup> , Daniela Cerezo-Wallis<sup>1,†</sup> , Cynthia Mucientes<sup>1</sup> , Tonantzin G Calvo<sup>1</sup>, Estela Cañón<sup>1,‡</sup>, Direna Alonso-Curbelo<sup>1</sup> , Nuria Ibarz<sup>2</sup>, Javier Muñoz<sup>2</sup> , José L Rodríguez-Peralto<sup>3</sup> , Pablo Ortiz-Romero<sup>4</sup> , Sagrario Ortega<sup>5</sup>  & María S Soengas<sup>1,\*</sup> 

## Abstract

Long-range communication between tumor cells and the lymphatic vasculature defines competency for metastasis in different cancer types, particularly in melanoma. Nevertheless, the discovery of selective blockers of lymphovascular niches has been compromised by the paucity of experimental systems for whole-body analyses of tumor progression. Here, we exploit immunocompetent and immunodeficient mouse models for live imaging of Vegfr3-driven neolymphangiogenesis, as a versatile platform for drug screening *in vivo*. Spatiotemporal analyses of autochthonous melanomas and patient-derived xenografts identified double-stranded RNA mimics (dsRNA nanoplexes) as potent inhibitors of neolymphangiogenesis, metastasis, and post-surgical disease relapse. Mechanistically, dsRNA nanoplexes were found to exert a rapid dual action in tumor cells and in their associated lymphatic vasculature, involving the transcriptional repression of the lymphatic drivers *Midkine* and *Vegfr3*, respectively. This suppressive function was mediated by a cell-autonomous type I interferon signaling and was not shared by FDA-approved antimelanoma treatments. These results reveal an alternative strategy for targeting the tumor cell-lymphatic crosstalk and underscore the power of *Vegfr3*-lymphoreporters for pharmacological testing in otherwise aggressive cancers.

**Keywords** dsRNA nanoplexes; GEMM melanoma models; *midkine*; neolymphangiogenesis; premetastatic niche

**Subject Categories** Cancer; Skin; Vascular Biology & Angiogenesis

**DOI** 10.15252/emmm.202012924 | Received 11 June 2020 | Revised 12 October 2021 | Accepted 15 October 2021 | Published online 11 November 2021

**EMBO Mol Med (2021) 13: e12924**

## Introduction

Clinical intervention in the cancer field has been revolutionized by the identification of (epi)genetic alterations in tumor cells as the basis for rational drug design (Van Allen *et al*, 2014). Prime example of this success is malignant melanoma, where BRAF mutations have led to the generation of effective inhibitors (Robert *et al*, 2019). Unfortunately, these targeted therapies are characteristically transient due to a plethora of mechanisms of resistance (Luebker & Koepsell, 2019; Rossi *et al*, 2019). Immune checkpoint blockers (e.g., anti-PD1, anti-PD-L1, or anti-CTLA4) are providing unprecedented response rates, particularly in combination with targeted therapies (Herrscher & Robert, 2020). Nevertheless, toxicities can be limiting, and median progression-free survival remains below 3 years (Herrscher & Robert, 2020). Therefore, the field is actively seeking for more effective agents to treat and prevent metastatic disease (Atkins *et al*, 2021). The expansion of the tumoral lymphatic vasculature (neolymphangiogenesis) is an attractive target for drug development, as this process is one of the earliest events in the dissemination of a variety of aggressive neoplasms (Achen *et al*, 2005; Stacker *et al*, 2014). Moreover, active mechanisms of crosstalk can be established between lymphatic endothelial cells and cancer cells that ultimately create tumor-permissive lymphovascular niches (Ma *et al*, 2018; Farnsworth *et al*, 2019). A variety of antibodies and small molecules have been developed to trap lymphangiogenic ligands (i.e., VEGFC/D) and/or block the interaction with and subsequent activation of their receptors (VEGFR family members) (Jain *et al*, 2006; Stacker & Achen, 2008; Zheng *et al*, 2014; Maisel *et al*, 2017). Still, none of these antilymphangiogenic treatments has been approved for clinical use, although they are being actively pursued in combination with targeted and immune-based therapies (Yamawaka *et al*, 2018). Compounds designed for a dual impact on the tumor cells and their associated pathogenic lymphatic vasculature have not yet been described.

1 Melanoma Laboratory, Molecular Oncology Programme, Spanish National Cancer Research Centre (CNIO), Madrid, Spain

2 Proteomics Unit, Biotechnology Programme, ProteoRed-ISCI, Spanish National Cancer Research Centre (CNIO), Madrid, Spain

3 Instituto de Investigación i+12, Hospital 12 de Octubre, Universidad Complutense Madrid Medical School, Madrid, Spain

4 Department of Dermatology, Hospital 12 de Octubre, Universidad Complutense Madrid Medical School, Madrid, Spain

5 Mouse Genome Editing Core Unit, Spanish National Cancer Research Centre (CNIO), Madrid, Spain

\*Corresponding author. Tel: +34 917 328 000; E-mail: dolmeda@cnio.es

\*\*Corresponding author. Tel: +34 917 328 000; E-mail: msoengas@cnio.es

†Present address: Spanish National Center for Cardiovascular Research (CNIC), Madrid, Spain

‡Present address: Memorial Sloan Kettering Cancer Centre, New York, NY, USA

A main limitation for the pharmacological assessment of antilymphangiogenic compounds has been the lack of animal models to define when and where lymphovascular niches are activated *in vivo* at distal premetastatic sites (Atkins *et al*, 2021; Patton *et al*, 2021). This has complicated longitudinal analyses of drug response, particularly after surgical removal of primary tumors, which may recapitulate adjuvant treatments that are under active clinical testing (Herrscher & Robert, 2020). In melanoma, a variety of genetically engineered mouse models (GEMMs) have been reported to recapitulate main genetic alterations in this disease, including, but not limited to, the activation of the *Braf* oncogene and the loss of the *Pten* tumor suppressor (Dankort *et al*, 2009; Dhomen *et al*, 2010). Crosses of these animals to various strains that allow for lineage tracing have been highly informative, for example, to define the cell of origin of melanomas (Kohler *et al*, 2017; Moon *et al*, 2017; Soengas & Patton, 2017; Sun *et al*, 2019). Nevertheless, these models do not have the sensitivity for the visualization of micrometastases *in vivo*.

Among lymphatic biomarkers, VEGFR3 represents an attractive candidate for drug screening using imaging techniques. VEGFR3 is highly expressed in lymphatic endothelial cells during development, but becomes downregulated in the adult, being maintained at low levels unless induced by pathological situations such as cancer (Petrova *et al*, 2008; Martinez-Corral *et al*, 2012). We have exploited this inducibility of VEGFR3 to develop melanoma “lymphoreporter” mice (Olmeda *et al*, 2017). These animals are based on a *knock-in* strategy whereby an EGFP-Luciferase cassette is coupled to the endogenous expression of *Flt4/Vegfr3* (Martinez-Corral *et al*, 2012). In particular, EGFP was useful to visualize the lymphatic vasculature in the embryo, while luciferase imaging allowed for longitudinal analyses of systemic tumor-associated neolymphangiogenesis in adult animals (Martinez-Corral *et al*, 2012). Moreover, spatiotemporal imaging of luciferase in these animals (herein referred to *Vegfr3<sup>Luc</sup>* for simplicity) revealed long-range-acting mechanisms of neolymphangiogenesis induced already at very early stages of tumor development. Specifically, *Vegfr3*-coupled luciferase imaging could be detected in sentinel lymph nodes and multiple visceral sites preceding melanoma metastasis; therefore, these mice were coined as *MetAlert* (Olmeda *et al*, 2017). These *MetAlert* mice, together with loss- and gain-of-function studies in melanoma cell lines and histopathological studies in human clinical biopsies, ultimately identified the growth factor Midkine (MDK) as a key driver of neolymphangiogenesis and metastasis (Olmeda *et al*, 2017). MDK is expressed in a variety of tumor types (Jono & Ando, 2010; Sakamoto & Kadomatsu, 2012; Sorrelle *et al*, 2017), but it had not been pharmacologically targeted to prevent lymphovascular premetastatic niche activation (Olmeda *et al*, 2017; Sorrelle *et al*, 2017). Therefore, these results highlighted the *MetAlert Vegfr3<sup>Luc</sup>*-lymphoreporters as a cost-effective platform for gene discovery (Hoshino & Lyden, 2017; Karaman & Alitalo, 2017; Perez-Guijarro & Merlino, 2017; Watch, 2017). Here, we define the potential of these mice for *in vivo* testing of anticancer agents. We characterized patient-derived xenografts and tumors induced by human melanoma cell transplants. In parallel, we used immunocompetent *Vegfr3<sup>Luc</sup>* mice for the assessment of autochthonous melanomas driven by oncogenic *Braf<sup>V600E</sup>* and *Pten* loss. Drug-induced responses were analyzed in two scenarios that recapitulate main clinical needs: (i) established melanomas and (ii) progressive

disease after surgical excision of primary lesions. This strategy identified a distinctive therapeutic action of dsRNA-based nanoparticles in blocking metastasis and preventing tumor relapse. Mechanistically, we found these dsRNA polyplexes to act by dual transcriptional inhibition of *MDK* and *VEGFR3* in both tumor cells and their associated activated lymphatic vasculature, respectively. While this study focused on melanoma, our results underscore the therapeutic potential of targeting the tumor–lymphatic crosstalk in other cancer types and support the *Vegfr3<sup>Luc</sup>* mice as a versatile platform for pharmacological screening of antimetastatic agents.

## Results

### Identification of a potent antilymphangiogenic activity of dsRNA mimics in *MetAlert*-lymphoreporter mice

Given the impact of neolymphangiogenesis on the conditioning and colonization of distal visceral sites in melanoma (Olmeda *et al*, 2017), we hypothesized that the “*MetAlert*-lymphoreporter” mice could serve as a tractable platform for preclinical studies of anticancer agents. To test autochthonous melanomas, immunocompetent *Vegfr3<sup>Luc</sup>* mice were crossed with *Tyr:CreERT2; Braf<sup>V600E</sup>; Pten<sup>fllox/fllox</sup>* (Dankort *et al*, 2009), a melanoma GEMM broadly used in the melanoma field (see a schematic of the reporter construct and the different strains used in this study in Fig 1A). *Vegfr3<sup>Luc</sup>* mice were also crossed into nude (*nu/nu*) mice as previously described (Olmeda *et al*, 2017), to generate hosts for whole-body imaging of tumors generated by human cell lines or human patient-derived xenografts (PDX; Fig 1A). To assess clinically relevant immunomodulators and genetically targeted agents, treatments were performed with a standard anti-PD-L1 ( $\alpha$ PD-L1) blocking antibody or with the BRAF inhibitor vemurafenib, respectively (Fig 1B). Treatments were first tested in the *Vegfr3<sup>Luc</sup>; Tyr:CreERT2; Braf<sup>V600E</sup>; Pten<sup>fllox/fllox</sup>* animals (herein referred to *Vegfr3<sup>Luc</sup>*-GEMM) where melanomas were induced by topical administration of 4-hydroxytamoxifen (5 mM, 3 consecutive days). Once melanomas reached ~20 mm<sup>2</sup>,  $\alpha$ PD-L1 antibody (10F.9G2, 200  $\mu$ g/dose, twice per week) or vemurafenib (50 mg/kg, seven doses per week) was administered systemically for 3 weeks as described in the Methods section. As shown in Fig 1B, both agents delayed tumor growth (see also Fig 1C), thus reducing *Vegfr3*-Luc emission. However, and as the case for a large set of patients in the clinic (Robert *et al*, 2019; Herrscher & Robert, 2020), this response was incomplete, as reflected by a residual *Vegfr3<sup>Luc</sup>* emission at the implantation site and, importantly, at distal lymphovascular niches (Fig 1B). Therefore, the *MetAlert Vegfr3<sup>Luc</sup>*-GEMM can be used to monitor drug response *in vivo*, but also emphasized the need for additional treatments with more durable efficacy.

We then questioned whether the *MetAlert* mice could identify compounds with a stronger antitumoral activity and, possibly, new modes of action. Lymphatic endothelial cells can secrete and respond to a variety of immunomodulators (Farnsworth *et al*, 2019), which in the context of aggressive tumors may contribute to immune tolerance (Alitalo & Detmar, 2012; Zheng *et al*, 2014). We considered of interest agonists of pathogen-activated molecular pattern receptors (PAMPs), particularly dsRNA sensors, as these compounds are being actively pursued for their ability to target tumor cells and shift immunologically “cold” into “hot” tumors (Aznar

et al, 2019; Hur, 2019). However, whether PAMP inducers impact on lymphovascular niches is unknown. We thus chose to study synthetic (poly)inosinic:polycytidylic acid. This is a mimic of long viral

dsRNA, which we had previously demonstrated that can be efficiently delivered to tumor cells when packed into bioavailable nano-complexes of about 100–150 nm (Besch et al, 2009; Tormo et al,

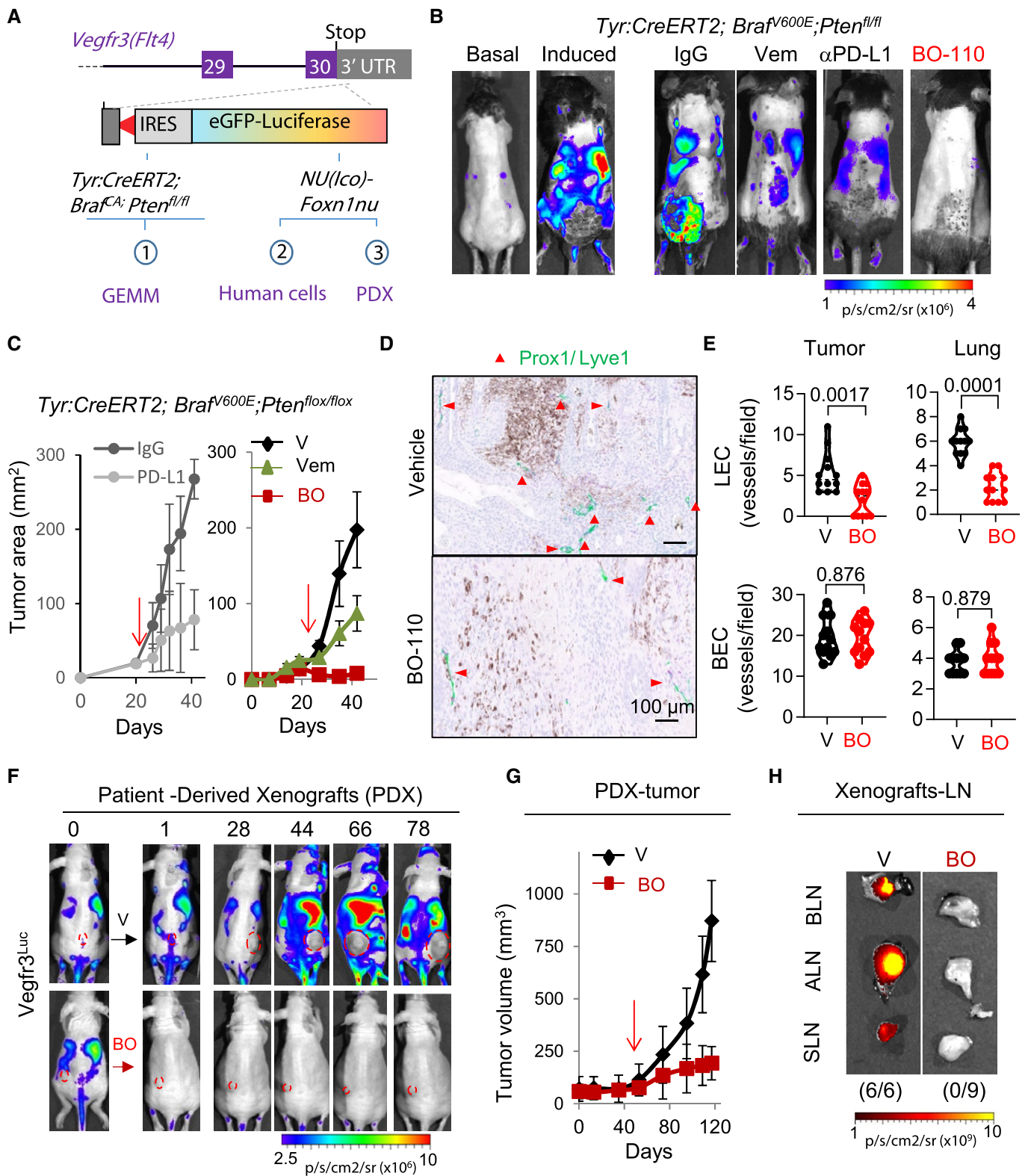


Figure 1.

### Figure 1. Identification of antilymphangiogenic compounds in *Vegfr3<sup>Luc</sup>* genetically engineered mouse models (GEMMs).

- A Schematic representation of the *Vegfr3<sup>Luc</sup>*-GEMM (*MetAlert*) mice to assess melanomas driven by melanocytic-specific induction of oncogenic *Braf<sup>V600E</sup>* in a *Pten*-deficient background (1), as well as to monitor xenografts of human cells (2) and patient-derived specimens (PDX, 3).
- B Luciferase-based imaging of drug response in *Vegfr3<sup>Luc</sup>;Tyr::CreERT2;Braf<sup>V600E</sup>;Pten<sup>flox/flox</sup>* mice. Panels labeled as "basal" and "induced" correspond to the bioluminescence of animals prior and 5 weeks after administration of 4OH-tamoxifen (5 mM, topical administration, 3 consecutive days) for the induction of melanomas. Right panels: Treatment with anti-PD-L1 antibody ( $\alpha$ PD-L1; clone 10F.9G2, 3 weeks) or the corresponding control IgG (200  $\mu$ g/dose, twice per week, 3 weeks); vemurafenib (Vem, 50 mg/kg, oral once per day, 3 weeks), or BO-110 (BO, 0.8 mg/kg, twice per week, 3 weeks). Scale: p/s/cm<sup>2</sup>/sr ( $\times 10^6$ ).
- C Growth curves of *Vegfr3<sup>Luc</sup>;Tyr::CreERT2;Braf<sup>V600E</sup>;Pten<sup>flox/flox</sup>* melanomas treated with  $\alpha$ PD-L1 or IgG (200  $\mu$ g/dose, 2 doses/week; left panel), or with vemurafenib (Vem, 50 mg/kg, daily dose), BO-110 (BO, 0.8 mg/kg, 2 doses/week) or vehicle control (V, daily dose) as indicated. Data correspond to the average tumor size  $\pm$  SD at the indicated time points. Red arrows mark the initiation of treatment ( $n = \text{min } 5$  mice per condition). Two-way ANOVA statistics.  $P = 0.0012$  ( $\alpha$ PD-L1),  $P = 0.0007$  (BO-110) and  $P = 0.0353$  (vemurafenib).
- D Histological visualization of lymphatic vessel density (dual Lyve1/Prox1 staining) in representative sections of tumors of *Vegfr3<sup>Luc</sup>;Tyr::CreERT2;Braf<sup>V600E</sup>;Pten<sup>flox/flox</sup>* melanomas in mice treated with vehicle (V) or 4 doses of BO-110 (BO, 0.8 mg/kg). Double-positive (Lyve1, Prox1) vessels were pseudocolored to green to ease the visualization. See also images for lung lymphatic vessels in Fig EV1C. Red arrowheads indicate Lyve1-Prox1-positive lymphatic vessels.
- E Quantification of lymphatic and blood vessels density in tumors and lungs of *Vegfr3<sup>Luc</sup>;Tyr::CreERT2;Braf<sup>V600E</sup>;Pten<sup>flox/flox</sup>* melanomas after treatment as indicated in B, C. Data correspond to the quantification of four fields per tumor, performed in biological triplicates. Statistical significance was determined by the Mann-Whitney *t*-test.
- F Treatment with BO-110 of human patient-derived xenografts (PDX) implanted in *Vegfr3<sup>Luc</sup> nu/nu*. 42 days after implantation (when systemic luciferase was detected), animals were randomized for treatment with vehicle (V) or with 0.8 mg/kg BO-110 (BO, twice per week), and luciferase emission was acquired at the indicated times. Scale, p/s/cm<sup>2</sup>/sr ( $\times 10^6$ ).
- G Quantification of the inhibitory effect of BO-110 (BO, 0.8 mg/kg, 2 doses/week I.P. administration, 11 weeks) on the growth of melanoma PDXs. Red arrows mark the initiation of treatment. Shown are mean tumor size in mm<sup>3</sup>  $\pm$  SD in biological triplicates. Statistical significance was determined by two-way ANOVA.  $P = 0.0009$ .
- H Representative sentinel, axillary, and brachial lymph nodes (SLN, ALN, and BLN, respectively) of mCherry-SK-Mel-147-driven xenografts in *Vegfr3<sup>Luc</sup> nu/nu* mice treated with vehicle (V) or four doses of BO-110 (BO, 0.8 mg/kg) and imaged for mCherry fluorescence to assess metastatic potential as a function of treatment. Numbers in parenthesis correspond to mice with positive metastases in at least one LN (lymph node) with respect to the total animals analyzed per condition. Scale, p/s/cm<sup>2</sup>/sr ( $\times 10^6$ ). See also Fig EV1D and E for images and quantification of lymphatic vessels in lymph nodes.

Source data are available online for this figure.

2009), herein referred to as BO-110. BO-110 is relevant, as a derivative (BO-112) is currently under clinical testing (Aznar *et al*, 2019), and information in its mode of action may also be of relevance for other dsRNA-based therapies (Ming Lim *et al*, 2013; Rapoport *et al*, 2014; Salazar *et al*, 2014). First, we tested BO-110 activity on autochthonous melanomas generated in the *Vegfr3<sup>Luc</sup>*-GEMM mice. As shown in Fig 1B, systemic treatment with BO-110 (0.8 mg/kg, intravenous injections, twice per week, 3 weeks) abrogated *Vegfr3<sup>Luc</sup>* emission and tumor growth in a significantly more efficient manner than vemurafenib or  $\alpha$ PD-L1 (Fig 1C; see additional detail in Expanded View Fig 1A). Histological staining for *Vegfr3* (Fig EV1B) and for the lymphatic markers *Prox1* and *Lyve1* confirmed the inhibitory effect of BO-110 in tumor-driven neolymphangiogenesis at the cutaneous melanomas (Fig 1D) or at distal organs (see lungs in Fig EV1C) of *Vegfr3<sup>Luc</sup>*-GEMM mice. Importantly, the inhibitory effect of BO-110 on lymphatic cells was selective, as we did not observe significant differences in blood endothelial cells neither in tumor sections nor in lungs (see quantifications in Fig 1E).

The *MetAlert* mice were also found highly informative in the immune-suppressed backgrounds. Thus, we could also visualize an effective inhibitory effect of BO-110 in *Vegfr3<sup>Luc</sup>* emission and tumor growth in the context of patient-derived xenografts (PDX) that were minimally expanded in culture (Fig 1F and G). Prelabeling well-characterized aggressive melanoma cell lines (SM-Mel-147) with fluorescent agents (mCherry), we could observe that this antitumoral activity of BO-110 resulted in an effective blockade of metastatic dissemination (see different lymph nodes in Fig 1H), also associated with inhibition of tumor lymphangiogenesis (Fig EV1D), again, without affecting the blood vasculature (Fig EV1E). Therefore, these results validate *Vegfr3<sup>Luc</sup>* reporters as a tractable platform for drug testing *in vivo*, and point to BO-110 as a distinct blocker of tumor-induced lymphovascular niches. Importantly, the antitumoral effect of BO-110 in the immune-compromised strains used here (which are T-cell-deficient) suggested additional roles of this

compound beyond reported effects of PAMP inducers on T-cell function (Aznar *et al*, 2019; Hur, 2019).

### Acute inhibitory action of BO-110 on prolymphangiogenic factors in lymphatic endothelial cells and melanoma cells

In the course of time-dependent analyses of BO-110 in the *MetAlert* mice, we observed a reduction of over 80% *Vegfr3<sup>Luc</sup>* emission 24 h after a single administration of BO-110, even before detectable effects on tumor size (see Fig 2A and B). This was the case both for autochthonous GEMMs (Fig 2A) and for xenografts of aggressive melanoma cells (see Fig 2B for mCherry-labeled SK-Mel-147). As a comparison, one dosing of  $\alpha$ PD-L1 antibody or BRAF inhibitor treatment showed virtually no effect on *Vegfr3<sup>Luc</sup>* emission (Fig 2A).

Being so acute and effective, we looked for potential unspecific effects of BO-110 that may be linked to luciferase stability, rather than on-target effects on neolymphangiogenesis. To this end, we tested the effect of BO-110 on melanoma xenografts where the luciferase signal was driven by an unrelated SV40 promoter, instead of by the endogenous *Vegfr3<sup>Luc</sup>*. As summarized in Fig EV1F, BO-110 had no effect on luciferase emission from this SV40 promoter, while parallel studies showed a nearly complete blockade of *Vegfr3<sup>Luc</sup>* signal (see Fig EV1G for quantifications). We therefore set to question the molecular basis underlying this rapid and effective antilymphangiogenic activity of BO-110.

We first questioned whether lymphatic endothelial cells (LECs) could directly uptake BO-110 and respond by repressing this receptor and blunt lymphangiogenesis. HLECs (human lymphatic endothelial cells) were then incubated with BO-110 for subsequent testing of dsRNA sensors and VEGFR3 expression (note that herein we use the standard *Vegfr3* and VEGFR3 nomenclature for mouse and human genes, respectively—this applying also to other genes tested in this study). For dsRNA recognition, we focused on the MDA5 helicase, as we had previously demonstrated that this protein

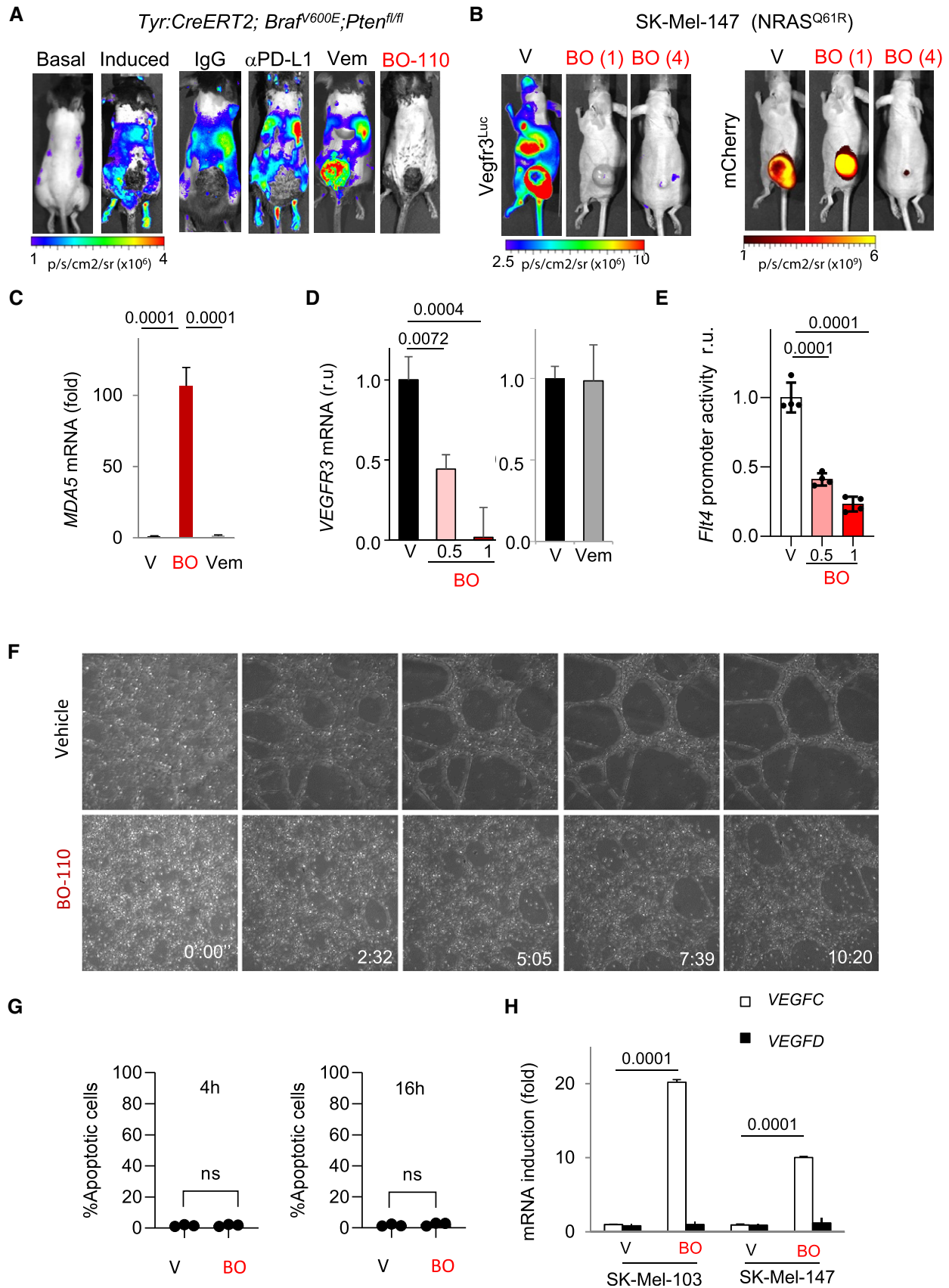


Figure 2.

**Figure 2. Inhibitory effects of BO-110 on prolymphangiogenic factors.**

- A Luciferase-based imaging of short-term drug response in *Vegfr3<sup>Luc</sup>;Tyr::CreERT2;Braf<sup>V600E</sup>;Pten<sup>flx/flx</sup>* mice. Panels labeled as "basal" and "induced" correspond to the bioluminescence of animals prior and 5 weeks after administration of 4OH-tamoxifen (5 mM, topical administration, three consecutive days) for the induction of melanomas. Right panels: images of mice that were treated the day before with one dose of the indicated compounds:  $\alpha$ PD-L1 antibody (clone 10F.9G2) or the corresponding control IgG (200  $\mu$ g/dose); vemurafenib (Vem, 50 mg/kg); or BO-110 (BO, 0.8 mg/kg). Scale: p/s/cm<sup>2</sup>/sr ( $\times 10^6$ ).
- B Response of xenografts of mCherry-labeled SK-Mel-147 in *Vegfr3<sup>Luc</sup>* nu/nu lymphoreporter mice treated with one dose (24 h) or 4 doses of BO-110 (BO, 0.8 mg/kg). Left panels correspond to *Vegfr3*-Luciferase (neolymphangiogenesis) and right panels to mCherry fluorescence emission (tumor content). Scale, *Vegfr3<sup>Luc</sup>*: p/s/cm<sup>2</sup>/sr ( $\times 10^6$ ) and mCherry: p/s/cm<sup>2</sup>/sr ( $\times 10^9$ ).
- C qRT-PCR analysis of relative mRNA levels of *MDA5* 16 h after treatment of HLEC with 0.5  $\mu$ g/ml BO-110 (BO), 10  $\mu$ M vemurafenib (Vem), or vehicle control (V). Data correspond to the mean  $\pm$  SD of three biological replicates. Statistical significance was determined by the t-test.
- D qRT-PCR analysis of relative mRNA levels of *VEGFR3* 16 h after treatment of HLEC with 0.5 or 1  $\mu$ g/ml BO-110 (VO), 10  $\mu$ M vemurafenib (Vem), or the corresponding vehicle control (V). Data correspond to the mean  $\pm$  SD of three biological replicates. Statistical significance was determined by ANOVA.
- E Luciferase signal driven by *FLT4* (*VEGFR3*)-promoter transduced into HLEC treated with vehicle (v) or BO-110 (BO) at the indicated doses ( $\mu$ g/ml) as indicated in Methods. Results were normalized to vehicle control. *N* = 4 biological replicates. Error bars correspond to mean  $\pm$  SD. Statistical significance was determined by ANOVA.
- F Tubulogenic activity of HLECs in the presence of BO-110. Images correspond to cells plated in Matrigel and imaged at the indicated time points after treatment with 0.5  $\mu$ g/ml BO-110. Complete time-lapse imaging of this process is shown in Movie EV1 (Appendix).
- G Analysis of apoptotic cells at the indicated time points. HLEC cells were treated with vehicle (V) or 0.5  $\mu$ g/ml BO-110 (BO) for the indicated time points. Cells were collected and apoptosis was analyzed by flow cytometry as indicated in Methods. Data correspond to the mean  $\pm$  SD of three experiments. Statistical significance was determined by the t-test.
- H Relative mRNA levels of *VEGFC* and *VEGFD* in the indicated melanoma cell lines 8 h after treatment with vehicle (V) or 0.5  $\mu$ g/ml BO-110 (BO), as determined by qRT-PCR. Data correspond to the mean  $\pm$  SD of three experiments. Statistical significance was determined by the t-test.

is a key effector of BO-110 in melanoma cells (Tormo *et al*, 2009). As a reference, we compared BO-110 with the BRAF inhibitor vemurafenib, because in other systems, this compound activates compensatory effects in the vasculature (Beazley-Long *et al*, 2015). Doses of these compounds were selected on the basis of previous analyses in melanoma cells (Tormo *et al*, 2009; Bollag *et al*, 2010). This strategy revealed that BO-110 resulted in a 100-fold increase of *MDA5* mRNA in LECs, while vemurafenib had virtually no effect (Fig 2C). Moreover, BO-110, but not vemurafenib, efficiently repressed *VEGFR3* mRNA (see *P*-values in Fig 2D). We demonstrated this repressive effect of BO-110 by cloning the *Flt4/VEGFR3* promoter into a luciferase-based reporter plasmid, and showing a 70% dose-dependent reduction in emission after treatment (Fig 2E).

Next, we tested the impact of BO-110 on the functionality of LECs, this assessed by monitoring the formation of tubulogenic structures in three-dimensional matrices (see Fig 2F for still images and Movie EV1 for a video in real time). Cell viability was analyzed in parallel, to rule out unspecific cytotoxic effects of BO-110 (Fig 2G). This strategy showed that BO-110 blocked LEC tube formation (Fig 2F) in conditions with no detectable impact on cell death (Fig 2G).

Being so potent as a blocker of neolymphangiogenesis, we considered the possibility of BO-110 acting also upstream of *VEGFR3*. We thus questioned classical activators of *VEGFR3* such as *VEGFC* and *VEGFD*, which can be secreted by aggressive tumor cells and play key roles in neolymphangiogenesis in cancer (Karaman & Detmar, 2014; Stacker *et al*, 2014). Intriguingly, RNA-based analyses (RT-PCR) indicated that melanoma-driven *VEGFD* was not altered by BO-110 (Fig 2H). Moreover, *VEGFC* was even induced by this compound (see quantifications for two melanoma cell lines in Fig 2H).

We then questioned the growth factor Midkine (MDK) as putative new target of BO-110. We interrogated MDK as this is a new inducer of neolymphangiogenesis and melanoma metastasis we recently described with prognostic features in human clinical biopsies (Olmeda *et al*, 2017). MDK was relevant as it is overexpressed in a broad variety of cancer types (Sorrelle *et al*, 2017), and no

pharmacological agents have been described to block its expression. BO-110 was found to reduce about 70–60% *MDK* mRNA levels in melanoma cell lines of different genetic backgrounds that recapitulate main protumorigenic mutations characteristic of this disease. Specifically, see Fig 3A for results in SK-Mel-147, expressing *NRAS<sup>Q61R</sup>* and Fig EV2A for data in 451LU; WM902B; (*BRAF<sup>V600E</sup>*; *PTEN<sup>WT</sup>*), SK-Mel-28 (*BRAF<sup>V600E</sup>*; *PTEN<sup>mut</sup>*; *P53<sup>mut</sup>*), or SK-Mel-103 (*NRAS<sup>Q61R</sup>*). This inhibitory effect of BO-110 on *MDK* was parallel to an induction of *MDA5* in all tested cell lines (see the corresponding quantifications and *P*-values in Figs 3B and EV2B). Importantly, this new activity of BO-110 on *MDK* was detected at early time points in which tumor cell viability was maintained over 80% (Figs 3C and EV2C). Cloning the *MDK* promoter into a reporter vector confirmed a direct inhibitory effect of BO-110 on *MDK* transcription (Fig 3D).

This repressive activity of BO-110 on *MDK* mRNA expression results in a marked, and also early, blockade of MDK secretion by melanoma cells (Fig 3E). Moreover, histological analyses demonstrated that BO-110 resulted in a potent abrogation of MDK expression *in vivo*, both in xenografts generated by human cell lines and from tumor biopsies (Fig 3F). Together, these data illustrate the versatility of *Vegfr3<sup>Luc</sup>* reporters to discover new mechanisms of action of anticancer agents, including repressors of tumor-driven MDK.

**IFN-based inhibition of MDK and VEGFR3 downstream of BO-110**

The results above illustrate a dual role of BO-110 repressing prolymphangiogenic factors both at the tumor and at the LEC level (via MDK and *VEGFR3*, respectively). These findings have translational implications because although various signaling cascades have been described to upregulate MDK or *VEGFR3* (Karaman & Detmar, 2014; Stacker *et al*, 2014; Zheng *et al*, 2014), repressors of these genes are less understood. In fact, to our knowledge, no mechanism has been reported to affect both genes at the mRNA level. We then started with RNA expression analyses in melanoma cells. Profiling SK-Mel-147 at early time points after BO-110 treatment (i.e., 4 and 10 h) revealed marked changes in the transcriptome of these cells

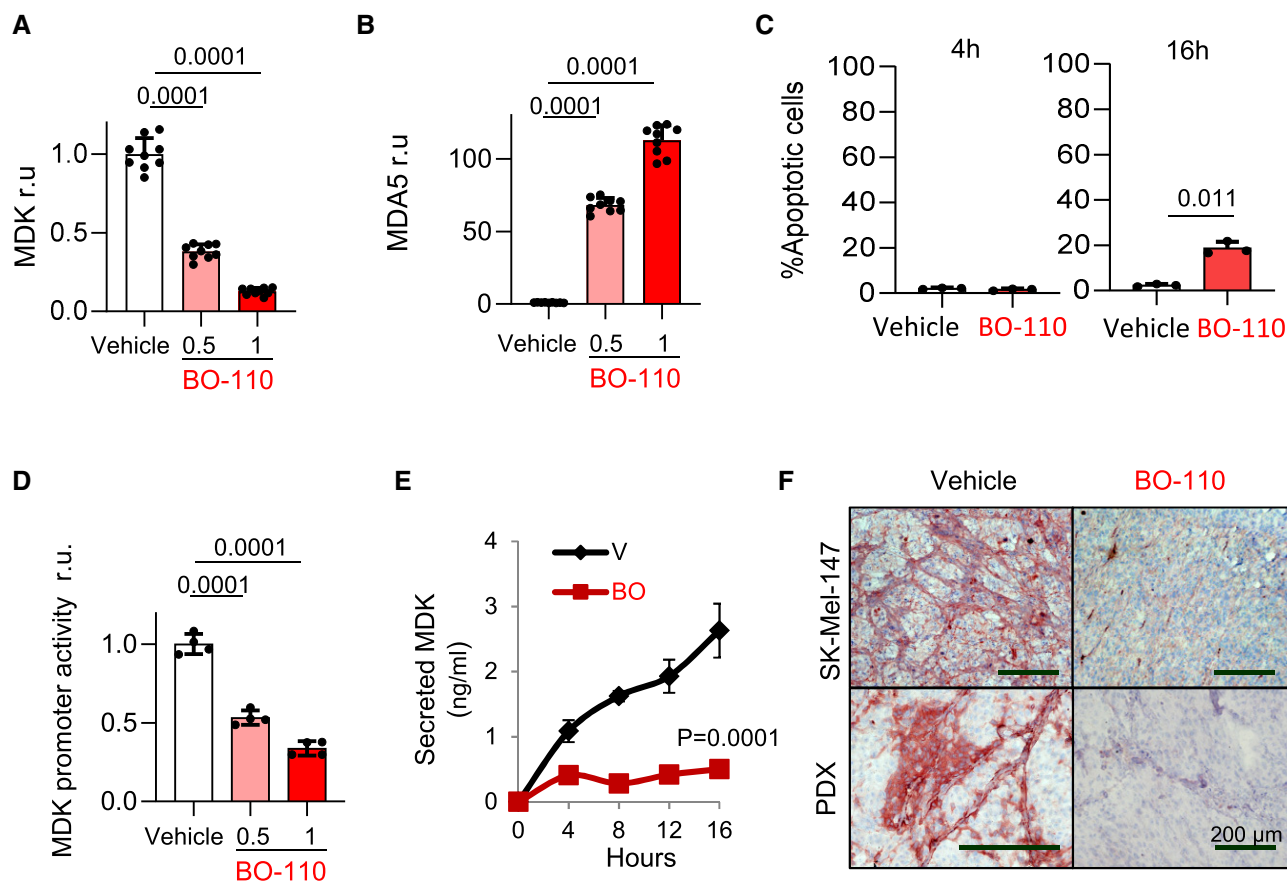


**Figure 3. Inhibitory effects of BO-110 on Midkine.**

- A Inhibitory effect of the indicated doses of BO-110 (in  $\mu\text{g/ml}$ ) or vehicle (V) on *MDK* mRNA expression determined by qRT-PCR in SK-Mel-147 (16 h after treatment). Data correspond to average mRNA levels in three experiments with technical replicates normalized to vehicle control  $\pm$  SD. Statistical significance was determined by ANOVA.
- B qRT-PCR analysis of relative mRNA levels of *MDA5* 16 h after treatment of SK-Mel-147 with the indicated doses of BO-110 (in  $\mu\text{g/ml}$ ) (BO). Data correspond to the mean  $\pm$  SD of three experiments with three technical replicates. Statistical significance was determined by ANOVA.
- C Analysis of apoptotic cells at the indicated time points. SK-Mel-147 cells were treated with vehicle (V) or 0.5  $\mu\text{g/ml}$  BO-110 (BO) for the indicated time points. Cells were collected, and apoptosis was analyzed by flow cytometry as indicated in Methods. Data correspond to the mean  $\pm$  SD of three experiments. Statistical significance was determined by the *t*-test.
- D Luciferase signal driven by *MDK* promoter transduced into SK-Mel-147 cells treated with vehicle (v) or BO-110 (BO) as indicated in Materials and Methods. Results were normalized to vehicle control. Data correspond to the mean  $\pm$  SD of four biological replicates. Statistical significance was determined by ANOVA.
- E MDK secretion by ELISA in SK-Mel-147 melanoma cells treated with vehicle (V) or 0.5  $\mu\text{g/ml}$  BO-110 (BO). Data correspond to the mean  $\pm$  SD of three biological replicates. Statistical significance was determined by two-way ANOVA.
- F Immunohistochemical analysis of MDK repression (pink staining) in SK-Mel-147 xenografts and PDX lesions after treatment with BO-110 (BO, 0.8 mg/kg, 2 doses/week). Histological staining in tumors extracted from animals treated with vehicle control (V) is included as a reference. Nuclei were counterstained with hematoxylin.

(Fig EV3A). These included the downregulation of a series of cell cycle-associated signaling cascades inhibited by BO-110, consistent with previous reports by our group and others on antiproliferative activities of dsRNA mimics (Tormo *et al*, 2009; Aznar *et al*, 2019). A variety of proinflammatory signals were also induced, enriched in particular, in interferon (IFN)-response pathways (Fig E3VA).

Although dsRNA mimics are well-known inducers of IFN-dependent transcriptional programs in cancer cells (Tormo *et al*, 2009; Aznar *et al*, 2019), melanoma cells (as other tumor cell types) express a variety of inhibitory feedback loops (Luke *et al*, 2017). Consequently, mRNA levels may not necessarily translate into significant effects in protein expression. To our knowledge, genome-

wide proteomic analyses have not been performed for dsRNA mimics in cells from tumors or other cell types. Therefore, proteomic analyses were performed by isobaric tag for absolute quantitation (iTRAQ) in SK-Mel-147, as well as in SK-Mel-28, to test melanoma cells of different genetic backgrounds. Differentially expressed genes were then assessed by GSEA through the Hallmarks (Fig 4A) and REACTOME (Fig 4B) gene set collections. Top ranking upregulated pathways in these analyses were related to type I-IFN, as well as to dsRNA sensors (*MDA5* and *RIG1*), as summarized in Fig 4A and B (see full lists of up- and downregulated gene sets in Datasets EV1 and EV2; FDR < 0.05). RT-PCR validated an efficient induction of *IFNA2* and most notably *IFNB1* by BO-110 in melanoma

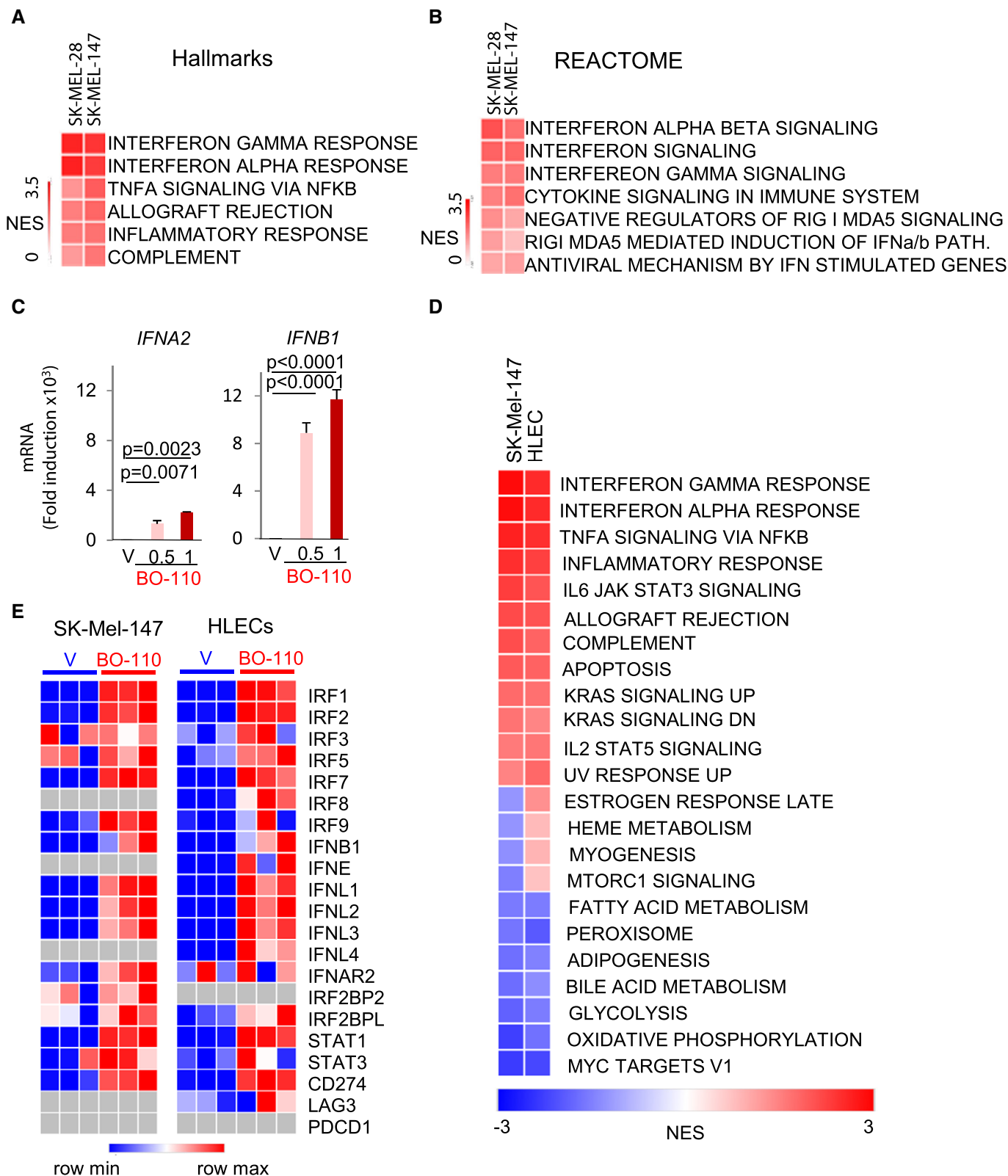


Figure 4.



#### Figure 4. High-throughput analysis reveals IFN induction as a key component of the BO-110 mechanism of action.

- A Heatmaps summarizing proteomic analyses (iTRAQ) performed in SK-Mel-28 and SK-Mel-147 after treatment with BO-110 (1  $\mu$ g/ml, 10 h). Shown are Hallmark gene sets with NES > 1. See also Datasets EV1 and EV2 for additional information.
- B REACTOME gene set analysis of protein changes in SK-Mel-28 and SK-Mel-147 cell lines treated with BO-110 (1  $\mu$ g/ml, 10 h).
- C Type I IFN mRNA induction (*IFNA2* and *IFNB1*) in SK-Mel-147 melanoma cells treated for 16 h with the indicated amounts of BO-110 (in mg/ml). Data correspond to the mean  $\pm$  SD of three experiments with three technical replicates normalized to vehicle control. Statistical significance was determined by ANOVA.
- D Heatmap showing differentially deregulated signaling cascades in SK-Mel-147 and HLEC treated with 1  $\mu$ g/ml BO-110 for 10 h (versus vehicle-treated controls). Data correspond to mRNA expression profiles analyzed by GSEA using the Hallmark gene sets. The scale indicates the normalized enrichment score (NES). See also Dataset EV3.
- E Heatmap depicting expression changes in interferon-related genes (GO:0034340) in SK-Mel-147 melanoma cells (left panel) and HLEC (right panel) treated with vehicle or 0.5 g/ml of BO-110 for 10 h. CD274, LAG3 and PDCD1 genes were also included as a reference.

cells (see for SK-Mel-147 in Fig 4C). Therefore, BO-110 can overcome intrinsic mechanisms of control of IFN signaling in melanoma cells.

Next, we interrogated the expression profile of hLECs to determine to which extent the response to BO-110 involved signaling cascades shared (or not) with melanoma cells, as a strategy to identify possible common modulators of MDK and VEGFR3 in the two cell types. GSEA using Hallmarks revealed an > 70% overlap of the pathways induced by BO-110 in both cell types (Fig EV3B; Datasets EV3 and EV4). These include various inflammatory and IFN-associated signals (Fig 4D). These data therefore illustrate the ability of BO-110 to contribute to immune modulation also at the level of the lymphatic vasculature. Analyses through the REACTOME dataset identified a broad spectrum of additional signaling networks deregulated by BO-110 in the two cell types (Fig EV3C; Datasets EV5 and EV6). Pathways involving mTOR signaling, estrogen response, or protein secretion were differentially regulated in HLEC and melanoma cells (see examples in Figs 4D and EV3 and full gene sets in Dataset EV5). Still, the overlap of pathways found by REACTOME in response to BO-110 of melanoma cells and HLEC was superior to 50% (Fig EV3C), emphasizing the reactive nature of these two cell types to BO-110. The top-5 upregulated gene sets found this approach both HLEC and SK-Mel-147 involved a large list of IFN-related factors that include a variety of cytokines and transcription factors (Fig 4D). Of note, BO-110 was found to induce immune checkpoint blockers (ICB) such as CD274 (PD-L1) in both cell types, and LAG3 additionally in HLECs (Fig 4E), which may be of interest for ongoing clinical trials of dsRNA-based agents in combination with various ICBs (Aznar *et al*, 2019; Kalbasi *et al*, 2020).

Importantly, and emphasizing acute (fast-acting) roles of IFN responses, we validated an over 1,000-fold induction of IFNB1 4h

after treatment in HLEC with similar kinetics than for melanoma cells (Fig 5A). Therefore, an attractive possibility was that this signaling cascade was responsive for the early coordinated repression of *VEGFR3* and *MDK* mRNA we found, respectively, in these two cell types. Therefore, we checked the INTERFEROME database (Rusinova *et al*, 2013) and the Encyclopedia of DNA Elements (ENCODE) (Davis *et al*, 2018) for genes regulated by IFN-related transcription factors in other systems. This approach revealed IFN-response elements in the promoters of *VEGFR3* and *MDK*, with binding sites for transcription factors such as IRF1, IRF7, IRF8, STAT1, or STAT3 (Fig EV4A), were induced by BO-110 in both cell types (Fig 4E).

To demonstrate the relevance of IFN- $\alpha/\beta$  signaling in the inhibitory effect of BO-110 on *MDK* and *VEGFR3*, we used blocking antibodies against IFN- $\beta$  or the IFN- $\alpha/\beta$  receptor chain 2 (IFNAR1). As shown in Fig 5B, these two blocking antibodies prevented the reduction of *MDK* expression by BO-110 in melanoma cells, even increasing its levels. Similarly, anti-IFN- $\beta$  or anti-IFNAR1 overturned the repression of *VEGFR3* mRNA by BO-110 in HLEC (Fig 5B), and rescued the tubulogenic activity of these cells, otherwise blocked by BO-110 (Fig 5C; see additional controls in Fig EV4B). Therefore, these results link BO-110 to *MDK* and *VEGFR3* mRNA expression via IFN signaling.

A corollary of the data above is that BO-110 should not be able to blunt tumor-induced neolymphangiogenesis in an IFN-defective background. To demonstrate this hypothesis, drug response was analyzed on mice that carry mono- or biallelic deletions of the IFN- $\alpha/\beta$  receptor 1 (*Ifnar1*) (Muller *et al*, 1994). The cell line used for tumor implants in these studies was B16-F10, isogenic to the B16 background of this *Ifnar1*-strain. Consistent with the multiple roles of IFN in immune surveillance (Hargadon, 2021), melanoma xenografts grew at a significantly faster rate in the homozygous *Ifnar*-

#### Figure 5. Mechanistic analyses of the repressive activity of BO-110 on melanoma-induced neolymphangiogenesis.

- A *IFNB1* mRNA induction analyzed by qPCR at the indicated times after BO-110 treatment (0.5  $\mu$ g/ml) of SK-Mel-147 melanoma cells or HLEC (left and right graphs, respectively). Data correspond to the mean  $\pm$  SD of three experiments with three technical replicates normalized to vehicle control.
- B Quantification of the impact of BO-110 as single agent or in the presence of the indicated blocking antibodies for type I interferon (IFNB1 or IFNAR1). Upper graphs show the effect of these agents on *MDK* mRNA levels in SK-Mel-147 melanoma cells. Similar treatments were performed on HLEC for the analysis of *VEGFR3* mRNA (middle graphs) and tube formation capacity (lower graphs). Data correspond to the mean  $\pm$  SD of 3 biological replicates in triplicate.
- C BO-110-driven blockade of the tube-forming capacity of HLEC and rescue with anti-IFNAR1 blocking antibodies. Images correspond to cells plated in Matrigel and imaged 8 h after treatment with 0.5  $\mu$ g/ml BO-110. See also Fig EV4B, for additional results with anti-IFNAR1 and anti-IFN- $\beta$  blocking antibodies.
- D Growth of B16 melanoma xenografts in siblings of *Ifnar1*<sup>+/+</sup>, *Ifnar1*<sup>+/-</sup>, or *Ifnar1*<sup>-/-</sup> mice. Treatment started 10 days after tumor cell implantation. BO-110 was administered at 0.8 mg/kg, every third day for 2 weeks. *N* = 6 mice per condition. Graphs show the mean tumor size  $\pm$  SD at each time point. Statistical significance was determined by two-way ANOVA.
- E Histological analyses of lymphatic vessel density by Lyve1 (blue) and Prox1 (purple) in representative lymph nodes of animals in (D) processed at the endpoint of the experiment (four doses of BO-110 or vehicle control). *N* = 6 mice per experimental condition. See Fig EV4C for a more complete view of these lymph nodes, where dual Prox1-Lyve1-positive cells were pseudocolored in red.

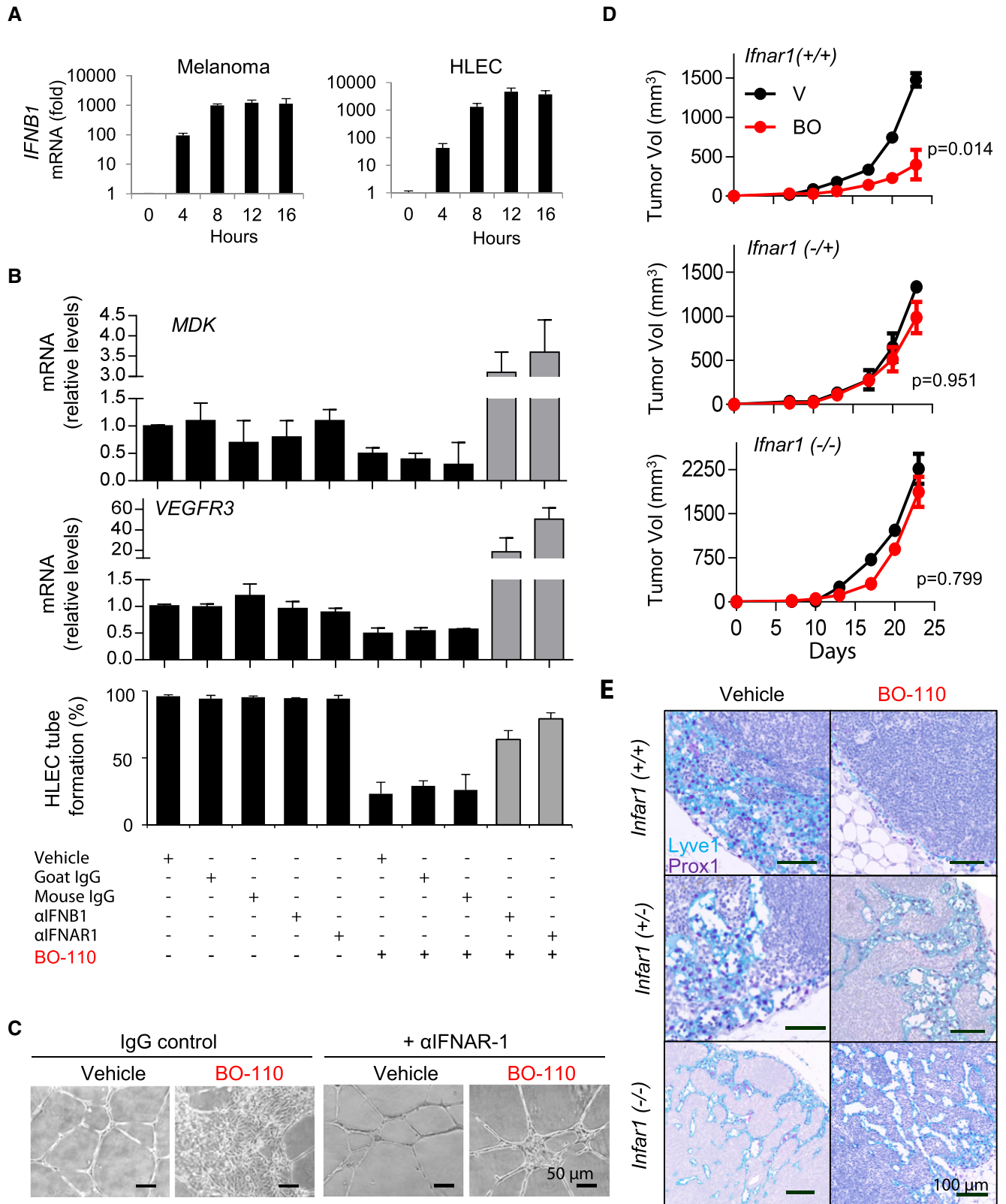


Figure 5.

deficient mice than in the heterozygous or wild-type littermates (Fig 5D). Interestingly, losing one copy of *Ifnar1* was already sufficient to nearly abrogate the ability of BO-110 to inhibit melanoma-

driven neolymphangiogenesis (see staining for Lyve1 and Prox1 in Fig 5E, and for more detail in Fig EV4C, and quantifications of this effect in Fig EV4D).

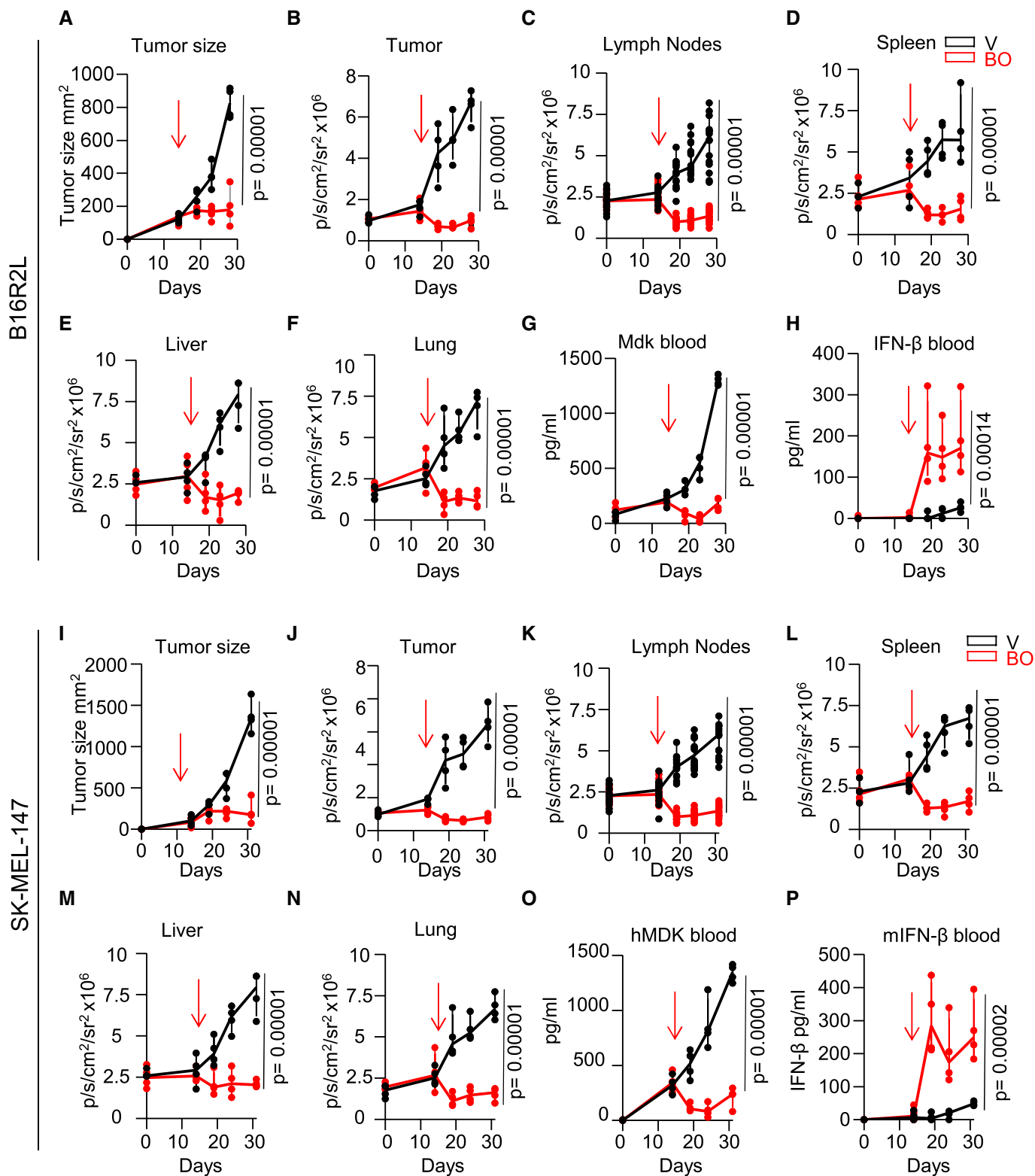


Figure 6.

**Figure 6. BO-110 induces a systemic interferon response that inhibits Mdk blood levels and tumor-induced lymphangiogenesis.**

- A Impact of BO-110 on tumor-bearing mice implanted with syngeneic B16R2L ( $5 \times 10^5$  cells). When tumors have an average size on  $100 \text{ mm}^3$ , mice were randomized into two groups and treated with BO-110 (BO) or vehicle (V), every second day for 2 weeks. The arrow indicates the start of the treatment. Tumor size was measured with a caliper at the indicated time points.
- B Quantification of Vegfr3<sup>Luc</sup> emission in the tumor area in mice in experiment (A).
- C Vegfr3<sup>Luc</sup> emission in the inguinal and brachial lymph nodes of mice in experiment (A).
- D–F Quantification of Vegfr3<sup>Luc</sup> emission in the spleen, liver, and lung of mice in experiment (A), respectively.
- G ELISA analysis of Mdk blood levels in mice in experiment (A).
- H ELISA analysis of mouse Ifn- $\beta$  blood levels in mice in experiment (A).
- I Antitumoral effect of BO-110 on xenografts of SK-Mel-147 ( $1 \times 10^6$  cells) implanted in the back of Vegfr3<sup>Luc</sup>; nu/nu nude mice. When tumors had an average size on  $150 \text{ mm}^3$ , mice were randomized into two groups and treated with BO-110 (BO, 0.8 mg/kg) or vehicle (V), every second day for 2 weeks. The arrow indicates the start of the treatment. Tumor size was measured with a caliper at the indicated time points, and tumor volume was calculated as indicated in Materials and Methods.
- J Quantification of Vegfr3<sup>Luc</sup> emission in the tumor area in mice in experiment (I).
- K–N Quantification of Vegfr3<sup>Luc</sup> emission in the lymph nodes, spleen, liver, and lung of mice in experiment (I), respectively.
- O ELISA analysis of Mdk blood levels in mice from (I).
- P ELISA analysis of mouse Ifn- $\beta$  blood levels in mice from (I).

Data information: For all panels in this figure,  $N = 4$  mice per condition. Statistical significance was determined by two-way ANOVA.

### Spatiotemporal analyses of drug response in the MetAlert mice

Collectively, the data above illustrate how the Vegfr3<sup>Luc</sup> MetAlert mice can be geared to the discovery of antilymphangiogenic factors, BO-110 in this case, with novel modes of action in tumor cells and HLEC, with an IFN-dependent inhibition of MDK and VEGFR3, respectively. The ability to monitor tumor-driven luciferase emission at the whole body level adds yet further versatility to these mice, for example, for otherwise quite challenging spatiotemporal pharmacological studies. Specifically, we set to test two clinically relevant aspects of the antitumoral activity of BO-110: (i) organ-dependent efficacies (namely, tumor vs lymph node and visceral sites), and (ii) the possibility of exploiting MDK as a biomarker of response in liquid biopsies (blood samples). To this end, we generated subcutaneous xenografts of high-MDK-expressing melanoma cells: the murine B16R2L (Fig 6A–H) and the human SK-Mel-147 (Fig 6I–P) for analyses of drug response in immune-competent and T-cell-deficient MetAlert mice, respectively. Treatment with BO-110 started when the cutaneous lesions were palpable (around  $100 \text{ mm}^3$ ; see arrows for all panels in Fig 6) and proceeded for 2 weeks. In the absence of BO-110, both of these lines are very aggressive as previously reported (Olmeda et al, 2017; Cerezo-Wallis et al, 2020). In these conditions, Vegfr3<sup>Luc</sup> emission correlated with tumor growth at the site of implantation (Fig 6B and J), and was induced systemically in the lymph nodes (Fig 6C and K), spleen (Fig 6D and L), lung (Fig 6F and M), and liver (Fig 6E and N). Both lines responded very efficiently to BO-110, reducing tumor growth and neolymphangiogenesis at the skin and all the organs tested (Fig 6A–F and I–N). Circulating MDK and IFN- $\beta$  were then assessed by ELISA in blood specimens collected at different time points from the control vs BO-110-treated groups. This approach revealed that MDK could indeed be detected in blood, reflecting tumor size (Fig 6G and O). Importantly, BO-110 acutely reduced circulating MDK (Fig 6G and O) with a concomitant induction of IFN- $\beta$  also occurring at early time points after treatment (Fig 6H and P). Note that for SK-Mel-147, the immunoadsorption assay detects the human form of MDK (i.e., not from the host), thus allowing to monitor tumor-driven effects of this protein. Therefore, these results support an efficient antitumoral activity of BO-110 exerted at the whole-body level, with tumor-secreted MDK as a biomarker of response

(more tightly associated with the melanoma cells than IFN, which can be produced by multiple tumor types).

### Long-term impact of BO-110 preventing metastatic relapse after surgery

One of the main clinical complications of primary melanomas is their potential for metastasis already from seemingly thin lesions. Thus, at the time diagnosis is performed and the cutaneous lesions are removed, tumor cells may be already be disseminated to distal organs (Khoja et al, 2015; Scatena et al, 2021). A main need in the field is to develop models to monitor this metastatic relapse after surgical excision (Patton et al, 2021). Therefore, we questioned whether monitoring neolymphangiogenesis via the Vegfr3<sup>Luc</sup> mice could serve as a platform to monitor (and attack) metastatic relapse after surgery. To this end, xenografts of human mCherry-labeled SK-Mel-147 melanoma cells were implanted subcutaneously. Primary lesions were excised when Vegfr3<sup>Luc</sup> was detectable in a systemic manner, at time points where micrometastases confirmed histopathologically in parallel studies in the lymph nodes (see Fig EV5) mimicking patients with melanomas at stage III that would be considered for adjuvant therapy (Han et al, 2021).

As shown in Fig 7A, surgery resulted in a progressive reduction in systemic Vegfr3<sup>Luc</sup> emission, consistent with the need for tumor-driven MDK secretion to activate premetastatic niches (Olmeda et al, 2017). Interestingly, Vegfr3-bioluminescence was regained with time (Fig 7A, right panels), and macrometastases ultimately developed as observed by monitoring tumor cell burden by mCherry fluorescence (Fig 7B). Importantly, 4 doses of BO-110 (every third day, starting 4 days after surgery) prevented both the re-acquisition of lymphangiogenesis and the subsequent tumor relapse (Fig 7A). Importantly, the efficacy of BO-110 was long-lasting, as 90% of animals remained tumor-free 8 months after treatment, whereas the average survival for the control group was 3 months (see Kaplan–Meier survival curves in Fig 7C;  $P = 0.0001$ ). Together, these results emphasize the versatility of Vegfr3<sup>Luc</sup>-GEMM reporter mice for non-invasive studies of melanoma initiation and progression, as well as a tractable platform for pharmacological screening of compounds to prevent and attack tumor metastasis.

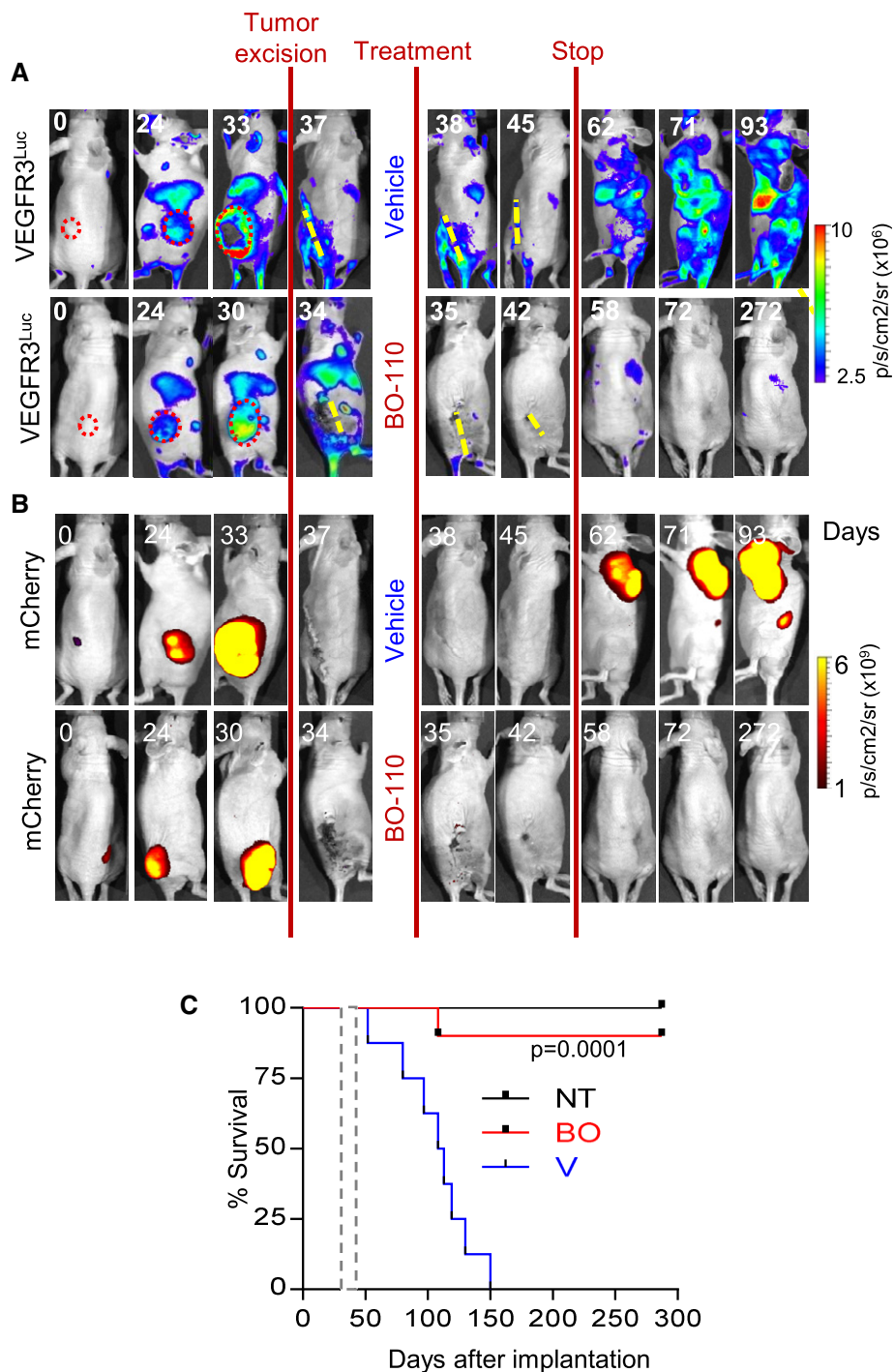


**Figure 7. BO-110 adjuvant treatment prevents metastatic melanoma relapse.**

**A** Efficacy of BO-110 as an adjuvant (preventing relapse after surgical removal of the primary lesion). Shown are representative examples of *Vegfr3<sup>Luc</sup>* mice implanted with mCherry-SK-Mel-147 and imaged for luciferase emission (prior to and after tumor removal). Animals were left to recover from surgery (4 days) and then treated for 2 weeks (four doses) with 0.8 mg/kg BO-110 or vehicle control ( $n = 8$  for control and  $n = 10$  for treatment arm). Scale, p/s/cm<sup>2</sup>/sr  $\times 10^6$ .

**B** mCherry emission from tumor cells of the animals in (A). Scale, p/s/cm<sup>2</sup>/sr  $\times 10^9$ .

**C** The Kaplan–Meier survival curves of animals treated as in (A). 8 of 8 animals treated with vehicle (V) control had to be sacrificed for humane reasons 110 days after surgery. 9 of 10 animals in the BO-110 arm (BO) remained tumor-free 8 months after stopping treatment. The gray box marks the period of treatment with BO-110. Statistical significance was determined by the logrank test.

## Discussion

Here, we present immunocompetent and immunodeficient *Vegfr3<sup>Luc</sup>* “MetAlert” mice as an *in vivo* screening platform for anticancer agents. Specifically, our data support the value of these models as a versatile resource for spatiotemporal analyses of drug response on established tumors, as well as in adjuvant settings that involve surgical excision of cutaneous lesions. The potential for the identification of potent antilymphangiogenic factors is illustrated by the discovery of unanticipated therapeutic activities of the dsRNA mimic BO-110 (see schematic in Synopsis). We had initially identified BO-110 as a potent inducer of hyperactivated autophagy in tumor cells (Tormo *et al*, 2009; Alonso-Curbelo & Soengas, 2010). The *Vegfr3<sup>Luc</sup>* reporters have now revealed an acute ability of BO-110 to blunt lymphangiogenesis at primary and distal sites, in conditions preceding tumor cell death. Guided by these results, we proceeded to a mechanistic study that ultimately uncovered a dual IFN-dependent repressive role of BO-110 on tumor cells (inhibiting MDK expression and secretion) and on lymphatic endothelial cells (repressing on *Vegfr3* mRNA levels). These functions are distinct from the reported action of lymphangiogenic factors in clinical testing (Stacker *et al*, 2014; Yamakawa *et al*, 2018), and were not recapitulated by FDA-approved therapies based on BRAF inhibition and checkpoint blockade. Of note, BO-110 did not promote detectable damaging effects on normal lymphatic vessels. Therefore, the *Vegfr3<sup>Luc</sup>* reporters have uncovered differential effects of dsRNA mimics not only in cancer cells and their associated vasculature, but on pathological versus normal lymphatic vessels as well. This information is timely, because a large range of factors have been found to promote lymphangiogenesis, but endogenous blockers of this process are less characterized (Farnsworth *et al*, 2019).

Perhaps one of the most unexpected results of this study was the finding that one single administration of BO-110 nearly abrogated *Vegfr3<sup>Luc</sup>* emission *in vivo* in melanomas of different genetic backgrounds. This information could potentially be used in clinical trials that are currently testing derivatives of BO-110 and other formulations of dsRNA (Ming Lim *et al*, 2013; Rapoport *et al*, 2014; Salazar *et al*, 2014; Aznar *et al*, 2019; Hur, 2019). For example, our data provide the proof of concept for using VEGFR3 and/or MDK inhibition (e.g., in needle biopsies of tumors or lymph nodes), as early markers to gauge drug delivery and response to dsRNA mimics in treated patients. In particular, our findings revealing circulating MDK as a biomarker that reflects reduced tumor burden after BO-110 treatment may prove useful to assess the antitumoral activity of this compound beyond less specific IFN-associated markers. Importantly, we have recently reported that MDK exerts potent immunosuppressive roles on macrophages and cytotoxic T cells (Cerezo-Wallis *et al*, 2020). Therefore, pharmacological blockade of MDK may have the added value of not only interfering with tumor neolymphangiogenesis and metastasis, but also impinging on the immune milieu.

It is tempting to speculate that the dual ability of BO-110 to target both MDK in cancer cells, and VEGFR3 in lymphatic cells, may represent an advantage with respect to other antilymphangiogenic agents. Thus, various tyrosine kinase inhibitors, VEGFC/D traps or VEGFR3-VEGFC/D interaction competitors, have been reported to interfere with VEGFR3 function (not its expression), but they exert incomplete responses or are limited by secondary toxicities (Stacker

*et al*, 2014; Yamakawa *et al*, 2018). In this context, it would be interesting to further address the multiple cytokines and immunomodulatory agents we found here to be under induced transcriptionally by BO-110 in both cell types, for combined treatments of BO-110 and immune checkpoint blockers.

The dual effect of BO-110 on VEGFR3 and of MDK via IFN signaling raises other practical considerations. For example, BO-110 and other dsRNA-based polyplexes are being actively pursued for their ability to (re)activate the innate immune system in aggressive cancers, with a particular interest in cytotoxic CD8<sup>+</sup> T cells, among others (Akira & Takeda, 2004; Hervas-Stubbs *et al*, 2011; Aznar *et al*, 2019). Here, we showed that even if T-cell functions were aberrant in patients (namely, recapitulating the *Foxn1<sup>tmu</sup>* nude mice used here), BO-110 would still be incorporated by tumors and lymphatic endothelial cells, activating IFN and blunting protumorigenic signals in both compartments.

Of note, this study focused on BO-110 and FDA-approved BRAF inhibitors and immune checkpoint blockers. However, the ability to monitor whole-body responses in the *Vegfr3<sup>Luc</sup>* mice could represent a cost-effective strategy to interrogate new compounds and drug combinations. Thus, these animals reveal when and where neolymphangiogenesis is induced *in vivo* and therefore can be used to set treatment regimens before or after this process is activated (i.e., to mimic preventing, adjuvant, or curative settings in the clinic). Moreover, it is important to consider that VEGFR3 and MDK are deregulated in a variety of tumor types and inflammatory diseases (Jones, 2014; Sorrelle *et al*, 2017; Weckbach *et al*, 2018; Yamakawa *et al*, 2018; Yuan *et al*, 2019). Therefore, data here expand the range of neoplasms where the *Vegfr3<sup>Luc</sup>* mice could be exploited for gene discovery and pharmacological analyses. This could include functional analyses of prolymphangiogenic factors identified in genomic screens that have yet to be validated (Williams *et al*, 2017). In addition, live imaging with the *Vegfr3<sup>Luc</sup>* mice could be used to assess other poorly understood functions of lymphatic endothelial cells in vascular patterning during development and wound healing, or a variety of pathologies that include type 2 diabetes and organ transplant, among others (Alitalo, 2011; Farnsworth *et al*, 2019). Similarly, assessing and importantly inhibiting MDK expression may also be of relevance in the context of proinflammatory roles of this protein in autoimmune and degenerative diseases (Aynacioglu *et al*, 2019; Herradon *et al*, 2019; Weckbach *et al*, 2019). The ability to compare immunocompetent and immunosuppressed backgrounds in the *Vegfr3<sup>Luc</sup>* MetAlert reporter adds yet further physiological relevance to whole-body imaging of lymphangiogenesis in basal conditions and pathogenic situations.

## Materials and Methods

### Mouse breeding, induction of nevi and melanomas in *Vegfr3<sup>Luc</sup>*-GEMM, and drug treatments *in vivo*

The *Vegfr3<sup>Luc</sup>* nu/nu immunodeficient mice and the *Vegfr3<sup>Luc</sup>*; *Tyr:CreERT2*; *Braf<sup>V600E</sup>*; *Pten<sup>lox/lox</sup>* animals were generated as described before (Olmeda *et al*, 2017) and maintained in a specific pathogen-free (SPF) area with a 12-h light–dark cycle at room temperature. All groups had ad libitum access to food and water throughout the whole study. Only females were used for experimentation to avoid

basal Vegfr3-Luc emission in testis. Specifically, strains used in this study are as follows: *Vegfr3<sup>EGFP/Luc</sup> (Flt4<sup>tm1.1Sgo</sup>)* (Martinez-Corral et al, 2012); *nu/nu (Cr1:NU(Ico)Foxn1<sup>nu</sup>)*; *Tyr::CreERT2/1Lru* (Yajima et al, 2006); *Braf<sup>CA</sup> (Braf<sup>tm1Mmcmt</sup>)* (Dankort et al, 2009); and *Pten<sup>tm2Mak</sup>* (Marino et al, 2002). Melanomas in the *Tyr::CreERT2* strains were induced in 14-week-old mice by topical treatment with 5  $\mu$ l of 5 mM 4-hydroxytamoxifen. BO-110 (a polyplex of pIC complexed with polyethylene imine) was prepared as described before (Tormo et al, 2009). When indicated, 0.8 mg/kg BO-110 was injected intravenously every 3 days (for a total of 4 administrations, unless indicated otherwise).  $\alpha$ PD-L1 antibody (Bioxcell, Lebanon, NH) was injected IP twice per week (200  $\mu$ g/dose) unless indicated otherwise. Vemurafenib (Selleck Chemicals, TX) was administered at 50 mg/kg (orally, once a day, during 3 weeks) as previously described (Yang et al, 2010). Animals were randomized into the different treatment arms before the start of the treatment. No blinding was performed.

### Non-invasive imaging of tumor growth and neolymphangiogenesis *in vivo*

Non-invasive imaging of luciferase in the *Vegfr3<sup>Luc</sup>*-GEMM was performed using an IVIS-SPECTRUM imaging system (PerkinElmer, Baesweiler, Germany) essentially as described before (Olmeda et al, 2017). Animals were anesthetized with isoflurane and injected intraperitoneally with 150 mg/kg luciferin (PerkinElmer). First, mCherry-tumor cell images were captured using the appropriate filters. Sequential images of luciferase emission were obtained every minute afterward, and the maximum light emission was determined for each animal as previously described (Martinez-Corral et al, 2012; Olmeda et al, 2017). Photons emitted from specific regions were quantified using Living Image software 4.3 (Perkin Helmer). *In vivo* luciferase activity is presented in photons per second per square centimeter per steradian (radiance). All experiments with mice were performed in accordance with protocols approved by the Institutional Ethics Committee of the CNIO and the Instituto de Salud Carlos III.

### Melanoma cells

Melanoma cells (SK-Mel-28, SK-Mel-147, 451LU, WM902B, B16R2L, and B16-F10), obtained from (ATCC), were cultured in DMEM (Invitrogen) supplemented with 10% FBS. All cell lines were authenticated using The GenePrint 10 System (Promega, MA). Cells were tested for mycoplasma contamination (Mycoplasma Detection Kit (LT07-318), Lonza, Basel, Switzerland) regularly and before injection in mice. When indicated, cells were stably infected with mCherry pLV-puro lentiviral vectors as described before (Tormo et al, 2009).

### Melanoma cell xenografts, patient-derived xenografts, and spontaneous metastasis assays

Xenografts of melanoma cell lines were generated in 14-week-old female *Vegfr3<sup>Luc</sup> nu/nu* mice by subcutaneous implantation of  $1 \times 10^6$  cells. Tumor growth was recorded by measuring the two orthogonal external diameters using a caliper. Tumor volume was calculated using the formula ( $a \times b^2 \times 0.52$ ). Tumors were excised

and processed for histological analysis when they reached 1.5 cm<sup>3</sup>. For spontaneous metastasis assays, SK-Mel-147 tumors were grown in the same conditions as described above until they reached a size of 1.2 cm<sup>3</sup>. Surgical excision was then performed under analgesics (buprenorphine 0.05 mg/day), and animals were left to recover for subsequent imaging of tumor growth and luciferase emission at increasing time periods. When indicated, treatments for the prevention of metastatic relapse were initiated 4 days after surgery.

Patient-derived xenografts (PDX) were generated from biopsies of skin metastases obtained from the Hospital 12 Octubre, Madrid, under their appropriate ethical protocols and provided to the investigators as anonymized lesions. These biopsies were excised into 4-mm cubes, embedded in Matrigel (BD), and implanted in the back of highly immunodeficient NSG mice (NOD. *Cg-Prkdc<sup>scid</sup> Il2rg<sup>tm1Wjl</sup>/SzJ*). Once the tumors reached 1,000 mm<sup>3</sup>, they were excised, processed again in 4-mm cubes, and reimplanted in the back of 3–6 NSG mice for amplification and subsequent reimplantation in *Vegfr3<sup>Luc</sup> nu/nu*.

### Histological analyses of gene expression in mouse tumors

Histological analyses of tissue architecture and expression of lymphangiogenic markers were performed on biopsies fixed in formalin and embedded in paraffin. Sections were prepared for hematoxylin-and-eosin (H&E) staining. For immunostaining, 3- $\mu$ m paraffin sections were deparaffinized and placed in PBS. Slides were incubated with the indicated primary antibodies as described below and developed with Ultravision ONE Detection System Kit (Thermo Scientific, TL-015-HAJ) using Permanent Mounting Medium (Prolong, Thermo Scientific). Analyses of lymphatic density were performed in an automated immunostaining platform (Autostainer (AS) Link 48, Dako, Agilent; Discovery XT, Ventana, Roche). For double Prox1/Lyve1 staining, antigen retrieval was first performed with a low pH buffer, and endogenous peroxidase was blocked with 3% peroxide hydrogen. Then, slides were incubated with goat anti-Prox1 (see provider below, at a 1/2,000 dilution). The slides were subsequently incubated with the corresponding secondary antibody (anti-goat) conjugated with horseradish peroxidase. The immunohistochemical reaction was developed in purple using 3, 30-diaminobenzidine tetrahydrochloride (FLEX DAB, Dako, Agilent). Next, for Lyve1 staining, antigen retrieval was performed with CC1 buffer (Ventana Medical Systems, Inc. Santa Clara, CA). Slides were then incubated with the rabbit anti-Lyve1 (1/250 dilution). After the incubation, slides were incubated with the corresponding secondary antibody (anti-rabbit) conjugated with horseradish peroxidase. The immunohistochemical reaction was developed in blue using Teal chromogen (Discovery Teal HRP Kit, Ventana Medical Systems). Nuclei were counterstained with Carazzi's hematoxylin. Slides were then dehydrated, cleared and mounted with a permanent mounting medium (Prolong, Thermo Fisher) for microscopic evaluation. For immunofluorescence, tissue sections were deparaffinized, incubated overnight with primary antibodies at 4°C in a humidified chamber, and then rinsed and incubated with fluorescent secondary antibodies for 1 h at room temperature. Nuclei were counterstained with Prolong Gold + DAPI (Invitrogen, concentration 5  $\mu$ g/ml).

Antibodies were used as follows:

Antibody	Code	Species	Dilution	Provider
mVegfr3	AF743	Goat	1:25	R&D Systems
mProx1	AF2727	Goat	1:2,000	R&D Systems
mLyve1	ab14917	Rabbit	1:250	Abcam
CD31	ab28364	Rabbit	1:250	Abcam
MDK	sc-46701	Mouse	1:50	Santa Cruz Biotechnology

### Lymphatic and blood vessel quantification and pseudocoloring

For tumor and lung lymphatic and blood vessel quantifications in tumors and lung sections, pictures were captured using an Olympus AX70 microscope (10× objective). The density of lymphatic endothelial cells was defined by dual Lyve1/Prox1 staining. Blood vessels were visualized with an anti-CD31 antibody (ab14917, Abcam). The amount of positive cells was estimated by different investigators blind to experimental conditions. A minimum of 4 areas per mice and organ and 3 mice per condition were counted.

In the case of lymph nodes, paraffin-embedded sections were stained for Lyve1 and Prox1 as indicated before and scanned using an Axio Scan.Z1 slide scanner using a 40× objective (Zeiss, Oberkochen, Germany). The number of positively stained pixels for Lyve1/Prox1 in relation to the total number of pixels in the lymph node image was quantified using Fiji (ImageJ) software (Rasband, W.S., ImageJ, U. S. National Institutes of Health, Bethesda, Maryland, USA). When indicated, cells with dual Lyve1 and Prox1 staining were pseudocolored using Photoshop CC2019 (Adobe Inc.) color-replace tool.

### Quantitative reverse transcription-PCR

RNA purification from melanoma tissue samples and real-time reverse transcription-PCR (qRT-PCR) were performed essentially as described (Tormo *et al*, 2009) using the following primers:

hVEGF-C	hVEGF-C-F	TGCCAGCAACTACTACCACAG
	hVEGF-C-R	GTGATTATCCACATGTAATTGGTG
hVEGF-D	hVEGF-D-F	GGAGGAAAATCCACTTGCTG
	hVEGF-D-R	GCAACGATCTTCGTCAAACA
hVEGF-R3 (Flt4)	hVEGF-R3-F	CAAGAAAGCGCTTCAGGTA
	hVEGF-R3-R	GCAGAGAAGAAATGCTGACG
IFN $\alpha$ 2	hIFNA2-F	TCCTGCTTGAAGGACAGACA
	hIFNA2-R	TCCTGCTTGAAGGACAGACA
IFN $\beta$ 1	hIFNB1-F	GCTAGAGTGGAATCCTAAG
	hIFNB1-R	ACAGCATCTGCTGGTTGAAG
MDA5	hMDA5-F	GCGCACACCGCAGAGTCCAA
	hMDA5-R	TCCACAGGCTCTCAGGCCG
18S	18S-F	TTGGAGGGCAAGTCTGGTG
	18S-R	CCGCTCCCAAGATCCAACCTA

### Functional analyses in human lymphatic endothelial cells (HLECs)

Normal human lymphatic microvascular endothelial cells (HMVEC-dLy) (Lonza, MD) referred in the text as HLEC were grown as tissue culture monolayers in EGM<sup>TM</sup>-2 medium supplemented with MV BulletKit (Lonza). For tube formation assays, three-dimensional cultures were prepared with  $2.5 \times 10^5$  cells seeded in MW6 plates covered by a layer of Matrigel (BD, NJ). When indicated, cells were pretreated for 12 h with 0.5  $\mu$ g/ml BO-110 or vehicle control. Treatment was maintained thereafter. Pictures were acquired 10 h after seeding the cells. Time-lapse videos were acquired in the same experimental conditions using a Leica Thunder widefield microscope with a 10× objective 0.45NA and LASX v3.7 acquisition software. Images were captured every 45 min. Videos were processed using Fiji (ImageJ) software. For fluorescence detection of HLEC in this time-lapse imaging, cells were labeled with CellTracker<sup>TM</sup> Green CMFDA Dye (Thermo Fisher, C7025, Waltham, MA) following the manufacturer's instructions.

### Proteomic analyses: iTRAQ and LC-MS/MS

For proteomic analyses, cells were cultured for 24 h in 10-cm culture plates and then treated with 0.5  $\mu$ g/ml BO-110 or vehicle control. For total cell extract profiling, proteins were subjected to isobaric labeling analysis using iTRAQ 8-plex as described before (Perez-Guijarro *et al*, 2016), using isobaric amine-reactive tag according to the manufacturer's instructions (AB SCIEX). Labeled samples were pooled and evaporated in a vacuum centrifuge. The sample was cleaned up using a Sep-Pak C18 cartridge (Waters). Eluted peptides were vacuum-dried and reconstituted in OFFGEL solution before electrofocusing with a 3100 OFFGEL Fractionator (Agilent). 24 fractions were collected. Peptides were separated by RP chromatography using a nanoLC Ultra System (Eksigent), directly coupled with an Impact (Bruker) mass spectrometer, equipped with a CaptiveSpray ion source. Two micrograms of each fraction was loaded onto a reversed-phase C18, 5  $\mu$ m, 0.1  $\times$  20 mm trapping column (NanoSeparations). The peptides were eluted at a flow rate of 300 nl/min onto an analytical column packed with ReproSil-Pur C18-AQ, 2.4  $\mu$ m, 75  $\mu$ m  $\times$  50 cm (Dr. Maisch GmbH), heated to 45°C. Solvent A was 4% ACN in 0.1% FA and Solvent B acetonitrile in 0.1% FA. Peptides were separated using the following gradient 0–2 min 2% B, 2–119 min 2–20% B, 119–129 min 20–34% B, 129–140 min 98% B, and 140–145 min 2% B. The spray voltage was set to 1.35 kV, and the temperature of the source was set to 180°C. The MS survey scan was performed at a spectrum rate of 2.5 Hz in the TOF analyzer (80–1,600  $m/z$ ). The minimum signal for triggering MS/MS was set to 500 counts. The 20 most abundant isotope patterns with  $z \geq 2$  and  $m/z > 350$  from the survey scan were sequentially isolated and fragmented using a collision energy of 23–56 eV as a function of the  $m/z$  value. Dynamic exclusion was set to 30 s using the *rethinking* option. Raw data were processed using Proteome Discoverer 1.4 and MaxQuant 1.5 using standard workflows, and results were filtered at 1% FDR.

### Assessment of cell death

Apoptosis was determined by staining cells with Annexin-V-APC (BD Biosciences Pharmingen, San Jose, CA, USA), TMRE



(tetramethylrhodamine ethyl ester; Sigma), and DAPI (4',6-diamidino-2-phenylindole; Sigma). To this end,  $4 \times 10^5$  cells were seeded in 6-well plates (Corning, NY, USA) and were incubated with BO-110 at the doses stated in the figure legends. After the indicated times, floating and adherent cells (these detached with trypsin) were centrifuged for 5 min at 300 g, followed by a PBS wash. Cells were then resuspended in prewarmed TMRE (37°C) 40 nM in  $1 \times$  PBS and incubated for 10 min in the dark. After centrifuging a 5-min spin at 300 g, the cells were resuspended in 200  $\mu$ l of Annexin-V binding buffer (10 mM HEPES/NaOH pH 7.4, 140 mM NaCl, 2.5 mM  $\text{CaCl}_2$ ) containing 0.1  $\mu$ g/ml Annexin-V and 0.5  $\mu$ g/ml PI, and incubated for 20 min at 4°C. Cells were then counterstained with DAPI 1  $\mu$ g/ml and analyzed by flow cytometry with a FACSCalibur (Becton, Dickinson and Company, BD Biosciences; USA). Data were analyzed using FlowJo Software V.10 (Tree Star Inc., Ashland, OR, USA).

### MIDKINE and *Flt4* (VEGFR3) promoter assays

The *MDK* promoter (encompassing 1,063 bp upstream and 204 downstream of the Midkine starting site; NM\_001012333; chr11+: 46358816-46360083) and the *Flt4* promoter (encompassing 1364 bp upstream and 19 downstream of the *Flt4* starting site; NM\_002020; chr5-: 180009187-180010570) were cloned into pNL2.1 vector (#N1061; Promega, MA). These reporter plasmids were transfected into SK-Mel-147 cells or HLEC. Cells were co-transduced with pGL4.52-Luc2 (#E1320; Promega) vector as transfection control. Luciferase activity was monitored 16 h thereafter (in the presence or absence of BO-110) using the Nano-Glo<sup>®</sup> Dual-Luciferase assay (#N1610; Promega). Cell viability was kept over 80% in all conditions analyzed.

### Type I IFN blocking assays

For type I interferon blocking assays, human IFN- $\beta$  blocking antibody (Clone AF814; R&D) and its corresponding isotype (Goat IgG, R&D Systems) were used at a concentration of 0.2  $\mu$ g/ml. Anti-Interferon- $\alpha/\beta$  Receptor Chain 1 Antibody (IFNAR1) (clone MAR1-5A3; Biolegend, CA) and its corresponding isotype (Mouse IgG2a, clone GC270; Millipore) were used at 0.1  $\mu$ g/ml. Where indicated, these reagents were added simultaneously with BO-110 to the culture media.

### ELISA analyses of IFN- $\beta$ and Midkine in mouse plasma

For the analysis of Ifn- $\beta$  and mouse Midkine in plasma,  $5 \times 10^5$  B16R2L cells (Liersch *et al*, 2012) were injected in the flank of 14-week-old female *Vegfr3<sup>Luc</sup>* immunocompetent mice. For circulating Ifn- $\beta$  and human Midkine,  $1 \times 10^6$  SK-Mel-147 cells were injected in the flank of 14-week-old female *Vegfr3<sup>Luc</sup>*; *nu/nu* mice as previously reported (Olmeda *et al*, 2017). In all cases, tumor growth was recorded by measuring the two orthogonal external diameters using a caliper. Tumor volume was calculated using the formula ( $a \times b^2 \times 0.52$ ). *Vegfr3-Luc* emission was measured in an IVIS system as indicated above. When tumors reached a size of 100 mm<sup>3</sup>, mice were randomized and treated with 0.8 mg/kg BO-110 or vehicle control. 500  $\mu$ l of blood was extracted 8 h after the indicated treatments. Blood was then allowed to clot at room temperature for 30 min. The clot was removed by spinning at 2,000  $\times$ g for 10 min

### The paper explained

#### Problem

Imaging of metastatic niches before and after treatment and pre- and post-surgical removal is a main need in the cancer field. This is particularly the case for malignant melanomas, where lesions barely of millimeters in depth have an intrinsically high metastatic potential. A large fraction of metastatic melanoma patients are or become resistant to current therapies. Therefore, a platform for pharmacological screens *in vivo*, and the identification of novel anticancer agents will have important basic and clinical implications.

#### Results

We have previously generated a “*MetAlert* mice” whereby (pre)metastatic niches can be visualized by whole-body imaging of the lymphatic vasculature (neolymphangiogenesis). Here, we used these mice as models for preclinical studies of anticancer agents. The *MetAlert* mice revealed an inefficient antilymphangiogenic activity of anticancer agents (inhibitors of BRAF of the immune checkpoint blocker PD-L1) with limited efficacy in clinical settings. Further screening identified nanoplexes of dsRNA (BO-110) as potent systemic antilymphangiogenic blockers, with activity observed just after a single administration. This acute effect of BO-110 was found with a dual repressive action on melanoma cells and the lymphatic vasculature, and we described the underlying mechanism via an IFN-driven repression of MDK and VEGFR3, respectively.

#### Impact

Live imaging of tumor progression and drug response can facilitate the identification of novel anticancer agents. Here, we discovered an unexpected dual role of the dsRNA mimic BO-110 in the control of MDK and VEGFR3, which, being so rapid, could aid in assessing drug uptake and therapeutic response in clinical trials. These results set the proof of principle for the *MetAlert* mice as a cost-effective platform for drug screening in melanoma, as well as in other diseases that involve a pathogenic activation of the lymphatic vasculature.

in a refrigerated centrifuge. The supernatant was collected and stored at  $-80^\circ\text{C}$  until analysis. ELISA determination of Midkine and Ifn- $\beta$  levels was performed in duplicates using the following kits: Mouse Mdk (Mouse Midkine ELISA Kit PicoKine<sup>™</sup>; EK2015, Boster, Pleasanton, CA), Human MDK (Human Midkine ELISA Development Kit, 900-K190, Peprotech Rocky Hill, NJ), and mouse Ifn- $\beta$  (Mouse IFN- $\beta$  DuoSet<sup>®</sup> ELISA, DY8234, R&D Systems).

### Bioinformatics analyses

GSEA tests were performed using GSEA 4.1 software (Broad Institute). Gene set collections were retrieved from annotations of the Broad Institute Library of Molecular Signature Databases v7.2 (MSigDB). Gene sets were tested for false discovery rate (FDR). After the Kolmogorov–Smirnov correction for multiple testing, only those pathways with FDR < 0.25 were considered as significant. Heatmaps were created by Morpheus Heatmaps (<https://software.broadinstitute.org/morpheus>).

### Statistical analyses

Cell proliferation and tumor growth were analyzed by one-way and two-way ANOVA, respectively. Survival curves were estimated with the Kaplan–Meier product-limit method and compared using

logrank test. *P*-values are indicated in each figure, with  $P < 0.05$  considered significant. For *t*-test parametric analyses, the normal distribution of the data was tested using the Shapiro–Wilk test. Statistical processing of transcriptomic and proteomic data was performed as previously described (Tormo *et al*, 2009; Karras *et al*, 2019). All statistical analyses were performed using GraphPad 8 software.

## Data availability

The cDNA array data for BO-119 discussed in this publication were generated as previously reported (Tormo *et al*, 2009), and are deposited in NCBI's Gene Expression Omnibus database, with accession number GSE14445. The RNAseq data are deposited also in NCBI's Gene Expression Omnibus database, with accession number GSE180629 (<https://www.ncbi.nlm.nih.gov/geo/>). The mass spectrometry proteomics data have been deposited to the ProteomeX-change Consortium via the PRIDE partner repository with the dataset identifier PXD007000 (<https://www.ebi.ac.uk/pride/>).

**Expanded View** for this article is available online.

## Acknowledgements

The authors thank previous and present colleagues in the CNIO Melanoma Group, particularly Damià Tormo and Lisa Osterloh for help and support at the initial stages of this study; José A Esteban (CSIC-UAM) for critical reading of this manuscript; Lionel Larue (INSERM; France) and Martin McMahon (Hunstan Cancer Center, USA) for the *Tyr:CreERT2* and *Braf<sup>CA</sup>* mouse strains, respectively; and Ignacio Melero at Hospital Clínico, Pamplona, Spain, for *Ifnar1*-deficient mice. The authors thank Isabel Blanco, Soraya Ruiz, and Virginia Granda (CNIO-Animal Facility Unit), Diego Megias (CNIO-Confocal Unit), and Eduardo José Caleiras and Patricia Gonzalez (CNIO-Histopathology Unit) for technical assistance. M.S.S. work is supported by grants SAF2017-89533-R funded by MCIN/AEI/10.13039/501100011033/ and by ERDF "A way to make Europe", project GCB15152978SOEN funded by the Fundación Científica AECC, "la Caixa" Foundation under the project codes HR17-00232 and HR20-00465, from the European Research Council (ERC) under the European Union's Horizon 2020 research and innovation programme (grant agreement No 884699)" and an Established Investigator Award by the Melanoma Research Alliance (MRA). D.O. is funded by grants PI18/01057 funded by Instituto de Salud Carlos III and co-funded by ERDF "A way to make Europe" and "Beca Leonardo a Investigadores y Creadores Culturales 2018 de la Fundación BBVA". The CNIO Proteomics Unit is part of ProteoRed Platform, PRB3-ISCI, supported by grant PT17/0019/0005, co-funded by ERDF "A way to make Europe". S.O. is also supported by a grant BFU2015-71376-R funded by MCIN/AEI/10.13039/501100011033/ and by ERDF "A way to make Europe".\*

## Author contributions

MSS and DO conceived and designed all the studies in this work. SO conceived and developed the *Vegfr3<sup>EGFP<sup>LUC</sup></sup>* (*Flt4<sup>tm1.1Sgo</sup>*) and *Vegfr3<sup>LUC</sup> nu/nu* mouse models. DO developed the protocols for the analysis of tumor-induced lymphangiogenesis *in vivo* (pre- and post-surgery, and pre-post-treatment with BO-110), and was in charge of the histological assessment of *Vegfr3*, *Lyve1*, *Prox1*, and *CD31*. DC-W contributed to the antimelanoma drug

treatment experiments and performed the treatments on *Ifnar1*-deficient models; she helped with data analysis of the *in vivo* experiments and revised the manuscript. PO-R and JLR-P provided fresh melanoma biopsies for the generation of PDX. NI and JM contributed to data analysis. TGC and EC were in charge of animal breeding and genotyping and provided technical assistance. CM cloned *MDK* and *FLT4* promoters. DA-C and CM contributed with technical assistance. The manuscript was written by MSS and DO, revised by SO and DA-C, and approved by all authors. MSS and DO supervised the project.

## Conflict of interest

María S. Soengas is a co-founder of BiOncotech Therapeutics (now Highlight Therapeutics), a biotechnology company interested in the development of dsRNA-based treatments for aggressive cancers. She does not sit on the administrative board nor is she involved in decisions regarding clinical trials or commercial development of Highlight Therapeutics's compounds.

## References

- Achen MG, McColl BK, Stacker SA (2005) Focus on lymphangiogenesis in tumor metastasis. *Cancer Cell* 7: 121–127
- Akira S, Takeda K (2004) Toll-like receptor signalling. *Nat Rev Immunol* 4: 499–511
- Alitalo A, Detmar M (2012) Interaction of tumor cells and lymphatic vessels in cancer progression. *Oncogene* 31: 4499–4508
- Alitalo K (2011) The lymphatic vasculature in disease. *Nat Med* 17: 1371–1380
- Van Allen EM, Wagle N, Stojanov P, Perrin DL, Cibulskis K, Marlow S, Jane-Valbuena J, Friedrich DC, Kryukov G, Carter SL *et al* (2014) Whole-exome sequencing and clinical interpretation of formalin-fixed, paraffin-embedded tumor samples to guide precision cancer medicine. *Nat Med* 20: 682–688
- Alonso-Curbelo D, Soengas MS (2010) Self-killing of melanoma cells by cytosolic delivery of dsRNA: wiring innate immunity for a coordinated mobilization of endosomes, autophagosomes and the apoptotic machinery in tumor cells. *Autophagy* 6: 148–150
- Atkins MB, Curiel-Lewandrowski C, Fisher DE, Swetter SM, Tsao H, Aguirre-Ghiso JA, Soengas MS, Weeraratna AT, Flaherty KT, Herlyn M *et al* (2021) The state of melanoma: emergent challenges and opportunities. *Clin Cancer Res* 27: 2678–2697
- Aynacioglu AS, Bilir A, Tuna MY (2019) Involvement of midkine in autoimmune and autoinflammatory diseases. *Mod Rheumatol* 29: 567–571
- Aznar MA, Planelles L, Perez-Olivares M, Molina C, Garasa S, Etxeberria I, Perez G, Rodriguez I, Bolaños E, Lopez-Casas P *et al* (2019) Immunotherapeutic effects of intratumoral nanoplexed poly I:C. *J Immunother Cancer* 7: 116
- Beazley-Long N, Gaston K, Harper SJ, Orlando A, Bates DO (2015) Novel mechanisms of resistance to vemurafenib in melanoma - V600E B-Raf reversion and switching VEGF-A splice isoform expression. *Am J Cancer Res* 5: 433–441
- Besch R, Poeck H, Hohenauer T, Senft D, Häcker G, Berking C, Hornung V, Endres S, Ruzicka T, Rothenfusser S *et al* (2009) Proapoptotic signaling induced by RIG-I and MDA-5 results in type I interferon-independent apoptosis in human melanoma cells. *J Clin Invest* 119: 2399–2411

\*Correction added on 7th December, after first online publication: The authors added missing funding information to the acknowledgements section.

- Bollag G, Hirth P, Tsai J, Zhang J, Ibrahim PN, Cho H, Spevak W, Zhang C, Zhang Y, Habets G et al (2010) Clinical efficacy of a RAF inhibitor needs broad target blockade in BRAF-mutant melanoma. *Nature* 467: 596–599
- Cerezo-Wallis D, Contreras-Alcalde M, Troulé K, Catena X, Mucientes C, Calvo TG, Cañón E, Tejedo C, Pennacchi PC, Hogan S et al (2020) Midkine rewires the melanoma microenvironment toward a tolerogenic and immune-resistant state. *Nat Med* 26: 1865–1877
- Dankort D, Curley DP, Cartlidge RA, Nelson B, Karnezis AN, Damsky Jr WE, You MJ, DePinho RA, McMahon M, Bosenberg M (2009) Braf(V600E) cooperates with Pten loss to induce metastatic melanoma. *Nat Genet* 41: 544–552
- Davis CA, Hitz BC, Sloan CA, Chan ET, Davidson JM, Gabdank I, Hilton JA, Jain K, Baymuradov UK, Narayanan AK et al (2018) The encyclopedia of DNA elements (ENCODE): data portal update. *Nucleic Acids Res* 46: D794–D801
- Dhomen N, Da Rocha DS, Hayward R, Ogilvie L, Hedley D, Delmas V, McCarthy A, Henderson D, Springer CJ, Pritchard C et al (2010) Inducible expression of (V600E) Braf using tyrosinase-driven Cre recombinase results in embryonic lethality. *Pigment Cell Melanoma Res* 23: 112–120
- Farnsworth RH, Karnezis T, Maciburko SJ, Mueller SN, Stacker SA (2019) The interplay between lymphatic vessels and chemokines. *Front Immunol* 10: 518
- Han D, van Akkooi ACJ, Straker 3rd RJ, Shannon AB, Karakousis GC, Wang L, Kim KB, Reintgen D (2021) Current management of melanoma patients with nodal metastases. *Clin Exp Metastasis* <https://doi.org/10.1007/s10585-021-10099-7>
- Hargadon KM (2021) The role of interferons in melanoma resistance to immune checkpoint blockade: mechanisms of escape and therapeutic implications. *Br J Dermatol* <https://doi.org/10.1111/bjd.20608>
- Herradon G, Ramos-Alvarez MP, Gramage E (2019) Connecting meta-inflammation and neuroinflammation through the PTN-MK-RPTPbeta/zeta axis: relevance in therapeutic development. *Front Pharmacol* 10: 377
- Herrscher H, Robert C (2020) Immune checkpoint inhibitors in melanoma in the metastatic, neoadjuvant, and adjuvant setting. *Curr Opin Oncol* 32: 106–113
- Hervas-Stubbbs S, Perez-Gracia JL, Rouzaut A, Sanmamed MF, Le Bon A, Melero I (2011) Direct effects of type I interferons on cells of the immune system. *Clin Cancer Res* 17: 2619–2627
- Hoshino A, Lyden D (2017) Metastasis: lymphatic detours for cancer. *Nature* 546: 609–610
- Hur S (2019) Double-stranded RNA sensors and modulators in innate immunity. *Annu Rev Immunol* 37: 349–375
- Jain RK, Duda DG, Clark JW, Loeffler JS (2006) Lessons from phase III clinical trials on anti-VEGF therapy for cancer. *Nat Clin Pract Oncol* 3: 24–40
- Jones DR (2014) Measuring midkine: the utility of midkine as a biomarker in cancer and other diseases. *Br J Pharmacol* 171: 2925–2939
- Jono H, Ando Y (2010) Midkine: a novel prognostic biomarker for cancer. *Cancers* 2: 624–641
- Kalbasi A, Tariveranmohabadi M, Hakimi K, Kremer S, Campbell KM, Funes JM, Vega-Crespo A, Parisi G, Champekar A, Nguyen C et al (2020) Uncoupling interferon signaling and antigen presentation to overcome immunotherapy resistance due to JAK1 loss in melanoma. *Sci Transl Med* 12: eabb0152
- Karaman S, Alitalo K (2017) Midkine and melanoma metastasis: a malevolent mix. *Dev Cell* 42: 205–207
- Karaman S, Detmar M (2014) Mechanisms of lymphatic metastasis. *J Clin Invest* 124: 922–928
- Karras P, Riveiro-Falkenbach E, Cañón E, Tejedo C, Calvo TG, Martínez-Herranz R, Alonso-Curbelo D, Cifdaloz M, Perez-Guijarro E, Gómez-López G et al (2019) p62/SQSTM1 fuels melanoma progression by opposing mRNA decay of a selective set of pro-metastatic factors. *Cancer Cell* 35: 46–63.e10
- Khoja L, Lorigan P, Dive C, Keilholz U, Fusi A (2015) Circulating tumour cells as tumour biomarkers in melanoma: detection methods and clinical relevance. *Ann Oncol* 26: 33–39
- Köhler C, Nittner D, Rambow F, Radaelli E, Stanchi F, Vandamme N, Baggolini A, Sommer L, Berx G, van den Oord JJ et al (2017) Mouse cutaneous melanoma induced by mutant BRAF arises from expansion and dedifferentiation of mature pigmented melanocytes. *Cell Stem Cell* 21: 679–693.e6
- Liersch R, Shin JW, Bayer M, Schwoppe C, Schliemann C, Berdel WE, Mesters R, Detmar M (2012) Analysis of a novel highly metastatic melanoma cell line identifies osteopontin as a new lymphangiogenic factor. *Int J Oncol* 41: 1455–1463
- Luebker SA, Koepsell SA (2019) Diverse mechanisms of BRAF inhibitor resistance in melanoma identified in clinical and preclinical studies. *Front Oncol* 9: 268
- Luke JJ, Flaherty KT, Ribas A, Long GV (2017) Targeted agents and immunotherapies: optimizing outcomes in melanoma. *Nat Rev Clin Oncol* 14: 463–482
- Ma Q, Dieterich LC, Detmar M (2018) Multiple roles of lymphatic vessels in tumor progression. *Curr Opin Immunol* 53: 7–12
- Maisel K, Sasso MS, Potin L, Swartz MA (2017) Exploiting lymphatic vessels for immunomodulation: rationale, opportunities, and challenges. *Adv Drug Deliv Rev* 114: 43–59
- Marino S, Krimpenfort P, Leung C, van der Korput HA, Trapman J, Camenisch I, Berns A, Brandner S (2002) PTEN is essential for cell migration but not for fate determination and tumorigenesis in the cerebellum. *Development* 129: 3513–3522
- Martinez-Corral I, Olmeda D, Dieguez-Hurtado R, Tammela T, Alitalo K, Ortega S (2012) *In vivo* imaging of lymphatic vessels in development, wound healing, inflammation, and tumor metastasis. *Proc Natl Acad Sci USA* 109: 6223–6228
- Ming Lim C, Stephenson R, Salazar AM, Ferris RL (2013) TLR3 agonists improve the immunostimulatory potential of cetuximab against EGFR head and neck cancer cells. *Oncimmunology* 2: e24677
- Moon H, Donahue LR, Choi E, Scumpia PO, Lowry WE, Grenier JK, Zhu J, White AC (2017) Melanocyte stem cell activation and translocation initiate cutaneous melanoma in response to UV Exposure. *Cell Stem Cell* 21: 665–678.e6
- Muller U, Steinhoff U, Reis LF, Hemmi S, Pavlovic J, Zinkernagel RM, Aguet M (1994) Functional role of type I and type II interferons in antiviral defense. *Science* 264: 1918–1921
- Olmeda D, Cerezo-Wallis D, Riveiro-Falkenbach E, Pennacchi PC, Contreras-Alcalde M, Ibarz N, Cifdaloz M, Catena X, Calvo TG, Cañón E et al (2017) Whole-body imaging of lymphovascular niches identifies pre-metastatic roles of midkine. *Nature* 546: 676–680
- Patton EE, Mueller KL, Adams DJ, Anandasabapathy N, Aplin AE, Bertolotto C, Bosenberg M, Ceol CJ, Burd CE, Chi P et al (2021) Melanoma models for the next generation of therapies. *Cancer Cell* 39: 610–631
- Pérez-Guijarro E, Karras P, Cifdaloz M, Martínez-Herranz R, Cañón E, Graña O, Horcajada-Reales C, Alonso-Curbelo D, Calvo TG, Gómez-López G et al (2016) Lineage-specific roles of the cytoplasmic polyadenylation factor CPEB4 in the regulation of melanoma drivers. *Nat Commun* 7: 13418
- Perez-Guijarro E, Merlino G (2017) Lymphangiogenesis: from passive disseminator to dynamic metastatic enabler. *Pigment Cell Melanoma Res* 30: 509–510
- Petrova TV, Bono P, Holnthoner W, Chesnes J, Pytowski B, Sihto H, Laakkonen P, Heikkilä P, Joensuu H, Alitalo K (2008) VEGFR-3 expression is restricted to blood and lymphatic vessels in solid tumors. *Cancer Cell* 13: 554–556

- Rapoport AP, Aqui NA, Stadtmauer EA, Vogl DT, Xu YY, Kalos M, Cai L, Fang H-B, Weiss BM, Badros A *et al* (2014) Combination immunotherapy after ASCT for multiple myeloma using MAGE-A3/Poly-ICLC immunizations followed by adoptive transfer of vaccine-primed and costimulated autologous T cells. *Clin Cancer Res* 20: 1355–1365
- Robert C, Grob JJ, Stroyakovskiy D, Karaszewska B, Hauschild A, Levchenko E, Chiarion Sileni V, Schachter J, Garbe C, Bondarenko I *et al* (2019) Five-year outcomes with dabrafenib plus trametinib in metastatic melanoma. *N Engl J Med* 381: 626–636
- Rossi A, Roberto M, Panebianco M, Botticelli A, Mazzuca F, Marchetti P (2019) Drug resistance of BRAF-mutant melanoma: review of up-to-date mechanisms of action and promising targeted agents. *Eur J Pharmacol* 862: 172621
- Rusinova I, Forster S, Yu S, Kannan A, Masse M, Cumming H, Chapman R, Hertzog PJ (2013) Interferome v2.0: an updated database of annotated interferon-regulated genes. *Nucleic Acids Res* 41: D1040–1046
- Sakamoto K, Kadomatsu K (2012) Midkine in the pathology of cancer, neural disease, and inflammation. *Pathol Int* 62: 445–455
- Salazar AM, Erlich RB, Mark A, Bhardwaj N, Herberman RB (2014) Therapeutic In-situ autovaccination against solid cancers with intratumoral poly-ICLC: case report, hypothesis, and clinical trial. *Cancer Immunol Res* 2: 720–724
- Scatena C, Murtas D, Tomei S (2021) Cutaneous melanoma classification: the importance of high-throughput genomic technologies. *Front Oncol* 11: 635488
- Soengas MS, Patton EE (2017) Location, location, location: spatio-temporal cues that define the cell of origin in melanoma. *Cell Stem Cell* 21: 559–561
- Sorrelle N, Dominguez ATA, Brekken RA (2017) From top to bottom: midkine and pleiotrophin as emerging players in immune regulation. *J Leukoc Biol* 102: 277–286
- Stacker SA, Achen MG (2008) From anti-angiogenesis to anti-lymphangiogenesis: emerging trends in cancer therapy. *Lymphat Res Biol* 6: 165–172
- Stacker SA, Williams SP, Karnezis T, Shayan R, Fox SB, Achen MG (2014) Lymphangiogenesis and lymphatic vessel remodelling in cancer. *Nat Rev Cancer* 14: 159–172
- Sun QI, Lee W, Mohri Y, Takeo M, Lim CH, Xu X, Myung P, Atit RP, Taketo MM, Moubarak RS *et al* (2019) A novel mouse model demonstrates that oncogenic melanocyte stem cells engender melanoma resembling human disease. *Nat Commun* 10: 5023
- Tormo D, Chęcińska A, Alonso-Curbelo D, Pérez-Guijarro E, Cañón E, Riveiro-Falkenbach E, Calvo TG, Larribere L, Megías D, Mulero F *et al* (2009) Targeted activation of innate immunity for therapeutic induction of autophagy and apoptosis in melanoma cells. *Cancer Cell* 16: 103–114
- Watch CDR (2017) A lymphoreporter mouse model identifies Midkine as a metastasis driver. *Cancer Discov* 7 <https://cancerdiscovery.aacrjournals.org/content/7/8/OF15>
- Weckbach LT, Grabmaier U, Uhl A, Gess S, Boehm F, Zehrer A, Pick R, Salvermoser M, Czermak T, Pircher J *et al* (2019) Midkine drives cardiac inflammation by promoting neutrophil trafficking and NETosis in myocarditis. *J Exp Med* 216: 350–368
- Weckbach LT, Preissner KT, Deindl E (2018) The role of midkine in arteriogenesis, involving mechanosensing, endothelial cell proliferation, and vasodilation. *Int J Mol Sci* 19: 2559
- Williams SP, Odell AF, Karnezis T, Farnsworth RH, Gould CM, Li J, Paquet-Fifield S, Harris NC, Walter A, Gregory JL *et al* (2017) Genome-wide functional analysis reveals central signaling regulators of lymphatic endothelial cell migration and remodeling. *Sci Signal* 10: eaal2987
- Yajima I, Belloir E, Bourgeois Y, Kumasaka M, Delmas V, Larue L (2006) Spatiotemporal gene control by the Cre-ERT2 system in melanocytes. *Genesis* 44: 34–43
- Yamakawa M, Doh SJ, Santosa SM, Montana M, Qin EC, Kong H, Han K-Y, Yu C, Rosenblatt MI, Kazlauskas A *et al* (2018) Potential lymphangiogenesis therapies: learning from current antiangiogenesis therapies-A review. *Med Res Rev* 38: 1769–1798
- Yang H, Higgins B, Kolinsky K, Packman K, Go Z, Iyer R, Kolis S, Zhao S, Lee R, Grippo J *et al* (2010) RG7204 (PLX4032), a selective BRAFV600E inhibitor, displays potent antitumor activity in preclinical melanoma models. *Can Res* 70: 5518–5527
- Yuan Y, Arcucci V, Levy SM, Achen MG (2019) Modulation of immunity by lymphatic dysfunction in lymphedema. *Front Immunol* 10: 76
- Zheng W, Aspelund A, Alitalo K (2014) Lymphangiogenic factors, mechanisms, and applications. *J Clin Invest* 124: 878–887



**License:** This is an open access article under the terms of the Creative Commons Attribution License, which permits use, distribution and reproduction in any medium, provided the original work is properly cited.